Investigation of the Properties of Ni–B/TiC Nanocomposite Coatings Produced at Different Particle Concentrations by Electrodeposition

ERSİN ÜNAL, ABDULKADİR YAŞAR, and İSMAIL HAKKI KARAHAN

In this experimental work, Ni–B/TiC nanocomposite coatings were deposited on a stainless steel substrate by conventional electrodeposition method and their features such as hardness, crystalline structure, corrosion and wear behavior were investigated. Furthermore, the same method was carried out in order to produce pure Ni and Ni–B alloy coatings and their properties were analyzed for comparison purposes. It was observed that nanocomposite coatings had much lower crystal grain size than pure Ni and slightly higher crystal grain size than Ni–B alloy. As a result of SEM analysis, it was determined that both B element and TiC particles were homogeneously deposited into the main structure, and the surface morphology was also affected by these components. According to the microhardness results, it was noted that the nanocomposite coating hardness with the highest hardness value increased by 160 pct compared to the pure Ni and 90 pct more than the Ni–B alloy. In the corrosion analysis, the corrosion resistance of nanocomposite coatings with TiC reinforcement improved significantly, and it was determined that the sample with 12 g/l TiC bath concentration performed 371 pct better than pure Ni and 440 pct better than Ni–B alloy in terms of corrosion current. Moreover, it was determined that the wear performance of nanocomposite coatings improved with increasing hardness and there was a 90 pct reduction in wear volume loss when compared to pure Ni.

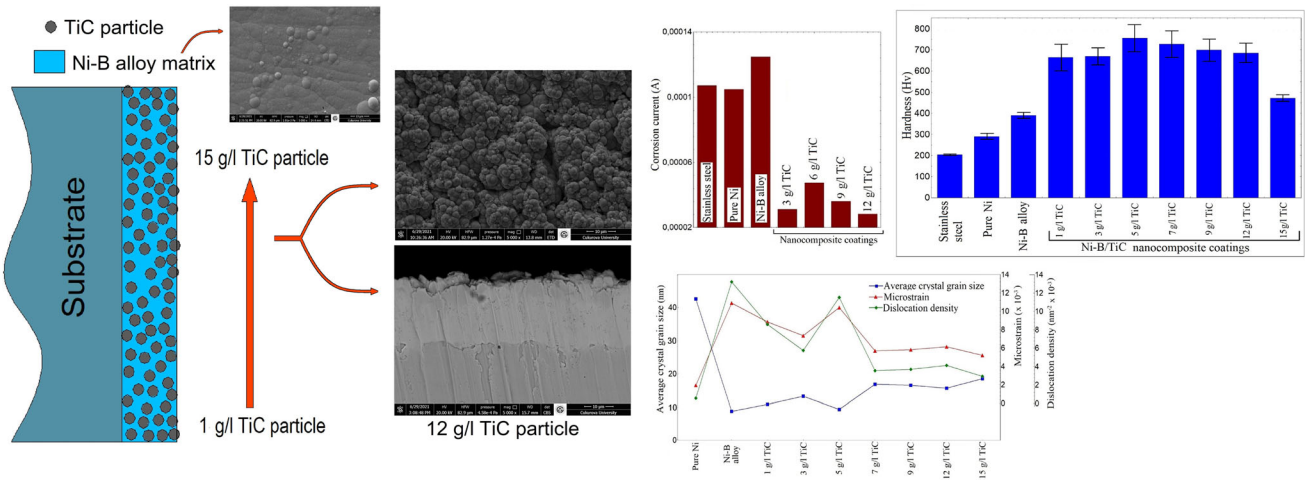

https://doi.org/10.1007/s11661-023-07020-0
© The Minerals, Metals & Materials Society and ASM International 2023

ERSİN ÜNAL is with the Department of Mechanical Engineering, Engineering Faculty, Osmaniye Korkut Ata University, 80000, Osmaniye, Turkey. ABDULKADİR YAŞAR is with the Department of Mechanical Engineering, Ceyhan Engineering Faculty, Çukurova University, 01190, Adana, Turkey. Contact e-mail: ayasar@cu.edu.tr İSMAIL HAKKI KARAHAN is with the Department of Physics, Faculty of Arts and Sciences, Mustafa Kemal University, 31040, Hatay, Turkey.

Manuscript submitted June 16, 2022; accepted February 15, 2023.
Article published online March 16, 2023

I. INTRODUTION

WEAR and corrosion of metals cause great economic losses every year. In terms of corrosion and wear resistance, effective reduction of metal loss and preservation of the original structure of the metal are possible with the use of surface treatment technology, thereby

ensuring the efficient operation of different mechanical equipment.[1] Materials used in engineering and industrial fields face harsh service conditions and are expected to be resistant to wear and corrosion under these conditions. Material damage, often in the form of corrosion, wear and fracture, begins at its surface, which can reduce its performance and service life. This is mainly because the surface is often first exposed to harmful influences. Therefore, surface modification or surface coating technology is widely used in the production process, especially to prevent the corrosion and wear process and delay the deterioration process of engineering equipments.[2,3]

Coating parts made of various materials is an important industrial process and many industrial products covered with functional thin films can be processed. One of the functional coatings is Ni–B alloy film and due to its superior properties, it finds application in many industries such as aviation, automotive, chemistry and electricity.[4,5] Ni–B alloys are of great interest owing to their excellent brazing, wear resistance, high temperature resistance and corrosion resistance. Electroless coating technique has been used in the last few decades to obtain such super performance alloy coatings. Electroless coating is mainly based on the principle of oxidation and reduction and is a preferred method for coating the surfaces of various materials, in a solution containing a strong reducing agent and metal ions, to reduce metal ions as metal and to form a dense coating. Electroplating, on the other hand, is based on the principle of electrolysis and under the influence of the electric field strength, metal ions take electrons from the cathode and as a result, metal is deposited on the substrate (cathode) surface. However, in the coating material prepared with electroless coating, the crystal cells in the upper parts of the coating are larger and not dense. Electroplating has higher production efficiency than electroless coating, and the wear resistance and hardness of the prepared coating material is better than that of electroless deposited coating material. The use of electrodeposition method is preferred in many respects to make metal alloy coating efficient and economical and to perform metal surface modification.[1,6,7]

Existing Ni metal or alloy coating materials may be difficult to meet some specific and demanding requirements, and therefore a variety of new structural and functional materials may be needed. Composite coatings can effectively extend and improve the service life and performance of conventional coatings compared with traditional alloy coating. Composite materials can provide functional diversification through hard ceramic particles embedded in the coating layer.[1,8] Although it is seen that there are studies on strengthening with reinforcement particles so as to improve the properties of Ni–B alloys, it can be said that it has not reached a sufficient level yet. Examples of these studies are WC,[9] Al_2O_3,[10,11] SiC,[12] hBN,[13,14] TiB_2,[15] B_4C,[1] TiN,[16] YSZ.[17]

Titanium carbide (TiC) is a chemical compound of Ti and C, with excellent physical and chemical properties such as high melting temperature (3150 °C), superior thermal and chemical stability, good corrosion, high hardness (3000 kg/mm^2) and wear resistance. It is mostly used in aerospace, automobile industries and special cutting tools *etc*. It is the preferred reinforcing particle material used in applications where safety is the main factor.[18] It is cubic crystal phase and black in color and has a density of 4.93 g/cm^3. In recent years, the use of TiC as composite coating reinforcement particles has been preferred in order to increase wear and corrosion resistance in different applications.[19,20] Li and Zhang[21] performed ultrasonic assisted deposition in their study in which they strengthened the Ni–B alloy with TiC particles. They investigated the effects of current density and deposition time and reported improvement in corrosion resistance with TiC reinforcement. They also stated that they obtained a smoother surface and fine crystalline structure thanks to ultrasonic assisted deposition. Li *et al*.[22] used the pulse electrodeposition technique in their study of Ni–B alloy main structure supported by a mixture of TiC and Y_2O_3 particles and examined the effects of different duty cycles on the properties of the coating. Dilek *et al*.[23] supported the Ni-W alloy main structure with TiC particles in submicron particle size and investigated its tribology and corrosion properties. The authors reported the effects of TiC bath concentration variation on the properties of composite coatings produced by pulsed electrodeposition technique.

It is obvious that further studies and investigation of different electrochemical parameters are needed in the electrodeposition of Ni–B alloy main structure by reinforcing with TiC. Due to the fact that there are so many production parameters that affect each other, it is necessary to carry out a lot of experimental and analysis studies to obtain an efficient coating material.[24,25] In our literature research, it was seen that the effects of particle bath concentration change, which is a very important parameter in terms of electrodeposition, on the properties of Ni–B/TiC nanocomposite coatings were not investigated. In this study, for the first time in the literature the effects of particle bath concentrations on the properties of Ni–B/TiC nanocomposite coatings were investigated in detail. It is expected that the development of this new coating type, which is obtained as a result of strengthening the Ni–B alloy coating, which already has an important place in industrial applications, with TiC is going to make significant contributions to the literature and the industry.

II. EXPERIMENTAL PROCEDURE

A. *Electrodeposition*

Ni–B/TiC nanocomposite coatings and, for comparison, pure Ni and Ni–B alloy coatings were deposited on a stainless steel (AISI 304) substrate. Conventional Watts-type nickel bath was used as base plating solution. Platinum wire rod was utilized as anode, stainless steel as cathode and saturated calomel electrode (SCE) as reference electrode. The stainless steel substrate surface used as the cathode is arranged to have an area of 4 cm^2. During deposition, the electrodes were placed vertically in the

bath and approximately 3 cm space was left between them. The shape of the electrode material is rectangular. Stainless steel substrates are sanded before depositions and the surface was cleaned of unwanted substances such as dirty and oil. Then, it was etched in 10 pct hydrochloric acid (HCl) aqueous solution for 1–2 minutes and then rinsed with distilled water and made ready for deposition. The chemicals used in the electrochemical production baths and their production parameters are given in Table I.[24] Table I also shows the purity degrees and functions of the chemicals besides them. The powder size of TiC particles used as reinforcement particles is below 500 nm. SEM image of TiC particles at 100,000 × magnification and EDS content analysis are given in Figure 1. It can be seen that powder grains of various sizes were agglomerated in nanometric sizes. Such agglomeration is inevitable in nanometer-sized powder piles. Ultrasonic mixing is a very effective method to eliminate this type of agglomeration, especially in electrodeposition production processes. The electrochemical bath was subjected to ultrasonic mixing for 30 minutes before deposition in order to solve the aggregation problem in nanometer-sized particles. Hielscher UP 200S brand and model device was used for ultrasonic mixing. The cycle value is set to 1 and the amplitude value is set to 70 pct (~ 22 kHz) during this process. In addition, the bath was mixed with a magnetic stirrer during the deposition process. Sodium dodecyl sulfate (SDS) was used as a surfactant to keep the particles in the electrolyte. The color of the bath ready before depositions turns into a completely black appearance due to TiC particles. The bath was freshly prepared again for each sample deposition. In the electrochemical deposition process, the bath was open to the ambient air. Electrodeposition setup and cell schema are given Figure 2. 608E model device of CH Instruments brand was used in all electrochemical deposition.

B. *Corrosion and Cyclic Voltametri (CV)*

In corrosion analysis, open circuit potential (OCP) and Potentiodynamic Polarization (PDP) methods were utilized and carried out in 3.5 pct sodium chloride (NaCl) aqueous solution. OCP curves were recorded for 3600 s to obtain a stable potential value. The Tafel experiments were implemented in the potential range from 0.25 V below the open circuit potential to 0.25 V above the potential range, at a scanning rate of 1 mV/s. The samples were kept in a solution containing 3.5 pct NaCl for 1 h to obtain a balanced potential value before performing the Tafel measurement. Already during this period, OCP curves were obtained. Corrosion tests were carried out at room temperature.[26] To determine the effects of bath components, analyzes of electrolytes were made with the cyclic voltammetry (CV) technique. The variation of the potential with time is called the scanning rate and in our CV experiments, the scanning speed was taken as 10 mV/s. In the graph, it was seen that the deposition on the cathodic side starts around − 0.7 V, the dissolution on the anodic side starts around − 0.4 V and ends around 0.4 V. Considering these matters, the potential range scanned in our CV experiments was chosen between − 1.2 V and 1.2 V. 608E model device of CH Instruments brand was used in all electrochemical analysis.

C. *Microhardness and Wear*

Future-TECH FM-700e brand and model device was used for micro-hardness measurements. In the measurement the microhardness values, 500-g load was applied on the sample for 10 s. Measurements were executed at least 10 different regions in each sample and the average of these measurements was accepted as the microhardness value. As a result of the microhardness measurements, the hardness values that deviated excessively from the average were not included in the general average of the sample. The analysis of the wear resistance of the produced Ni–B/TiC nanocomposite coatings and the pure Ni coating for comparison purposes was carried out by ball-on-disk method and stainless steel was used as the ball material. For wear tests, Turkyus brand POD&HT&WT model (Turkey) wear analysis device was utilized. The wear test was carried out under a load of 2 N and was carried out at a

Table I. Bath Components and Deposition Parameters

Bath Components	Mission	Amount
$NiSO_4.6H_2O$ (Nickel Sulfate Hexa Hydrate) pct 99.99	source of nickel	240 g/l
$NiCl_2$. $6H_2O$ (Nickel Chloride Hexa Hydrate) pct 98	source of nickel	45 g/l
H_3BO_3 (Boric Acid) pct 99.5	complexing agent	30 g/l
Trimethylamine Borane Complex (TMAB) pct 97	source of boron	3 g/l
Titanium Carbide Powder (TiC) pct 99 Nano Size	reinforcement particle	0–15 g/l
Sodium Dodecyl Sulfate (SDS) pct 99	surfactant	0.5 g/l
Saccharin pct 98	grain reducer	2 g/l
Depositions Parameters		**Value**
Current Density		50 mA/cm^2
pH		4
Temperture		43 ± 1 °C
Time		60 min
Bath Mixing Speed		200–300 rpm
Ultrasonic Mixing Time Before Deposition		30 min

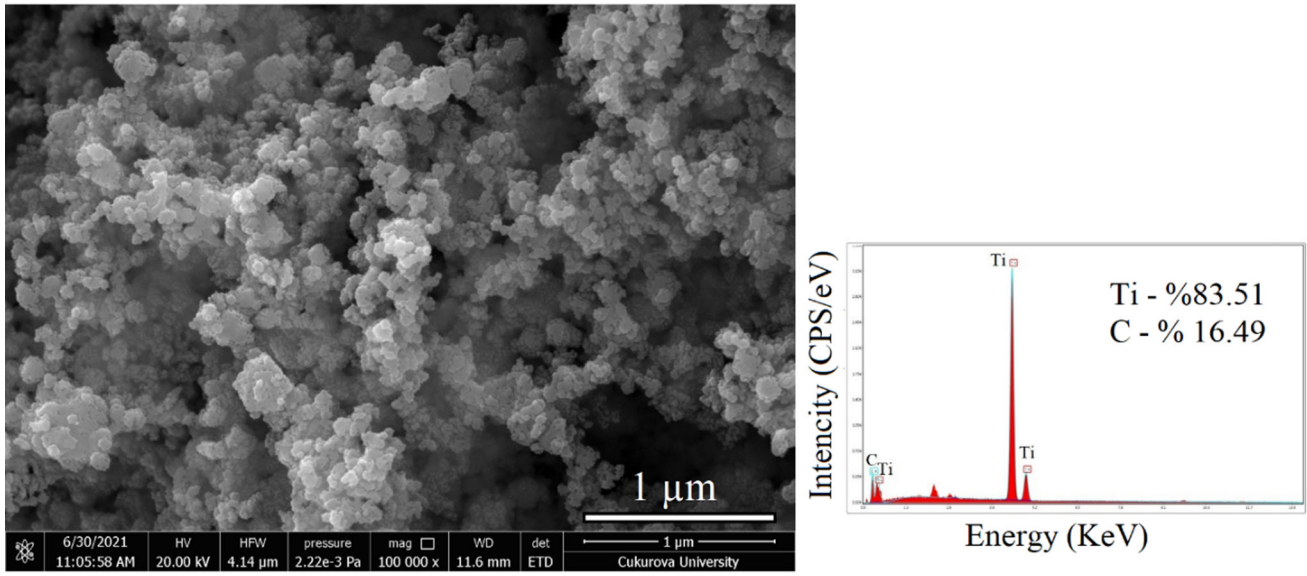

Fig. 1—SEM image and EDS analysis of TiC particles.

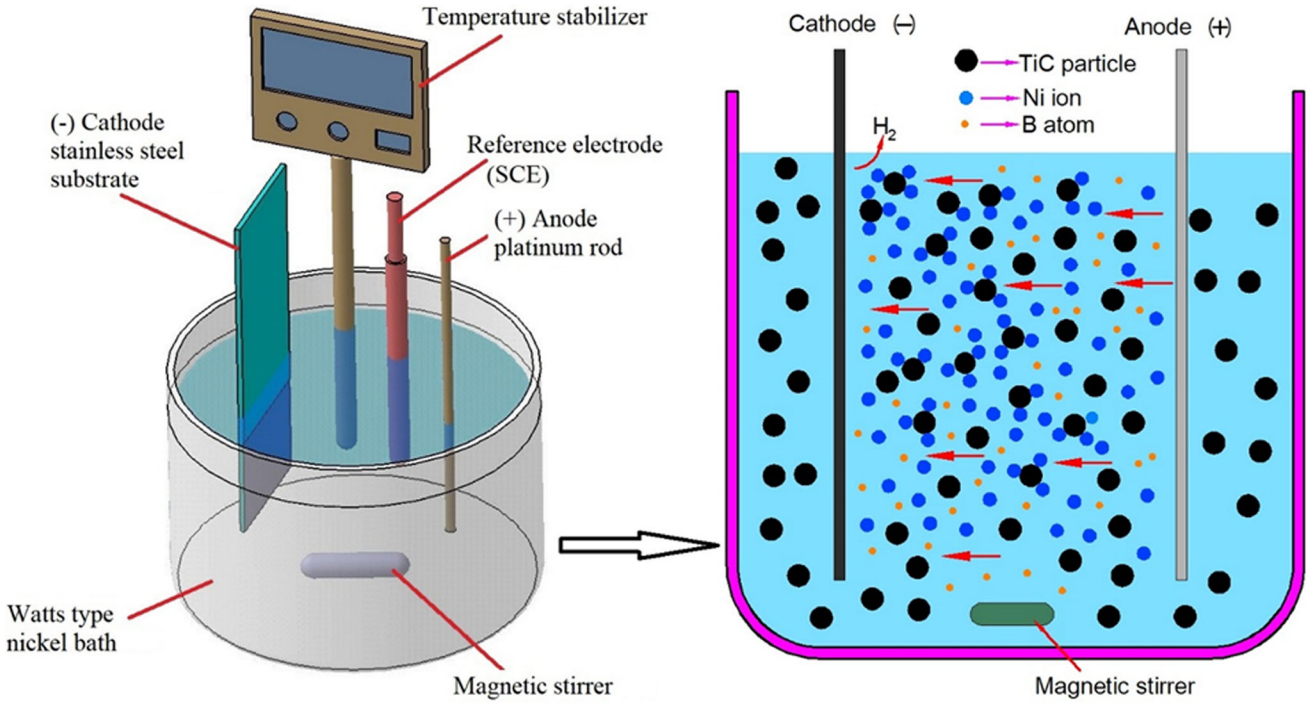

Fig. 2—Electrodeposition setup and cell schema.

speed of 0.25 m/s. In the abrasion test performed at room temperature, the trace diameter was set as 10 mm and its duration was limited to 400 s. The diameter of the stainless steel ball used as counter material is 6 mm. Wear volume loss values were calculated by using the average of the wear scar width and depth values obtained from the surface roughness profiles measured from 3 different regions of the wear scar, with the help of the formulas given below.

$$V = \frac{\pi . W . D . L}{4} \quad [1]$$

$$L = 2 . \pi . r \quad [2]$$

In the given formulas, V is the wear volume loss (mm^3), W is the average wear track width (mm), D is the

average wear track depth (mm), L is the wear track length (mm), r is the wear track radius (mm).[27–29] The roughness measurements of the wear marks were made with a Fimmetrics brand Profilm 3D model device.

D. *SEM and XRD*

SEM analyzes were performed with FEI brand Quanta 650 Field Emission model device. EDS and mapping analyzes were also executed with the same device. XRD patterns of the samples were obtained so as to characterize the crystal structures. PANalytical brand, Empyrean model XRD device, which produces CuKα radiation in the range of 2θ = 0–100 deg, at 40 kV and 30 mA values, was used (λ = 1.5418 Å) in order to reach X-ray diffraction patterns. The formulas given below were used while calculating the average crystal grain size (D), microstrain (ε) and dislocation density (δ) values of the samples.[30–37]

$$D = \frac{0.94\lambda}{\beta \cos\theta} \quad [3]$$

In the Debye–Scherrer Eq. [3], λ is the X-ray wavelength, β is the value in radians of the half-maximum width of the corresponding peak (FWHM), θ is the Bragg reflection angle of the corresponding peak.[37]

$$\varepsilon = \frac{\beta}{4 \tan\theta} \quad [4]$$

Equation [4] was used in the calculation of microstrain.[30,31]

$$\delta = \frac{1}{D^2} \quad [5]$$

Equation [5] was used to calculate the dislocation density. Here D denotes the mean crystal grain size.[30,34–36]

III. RESULT AND DISCUSSION

A. *Electrochemical Analysis of Ni–B/TiC Nanocomposite Deposition Baths*

CV graphs of Ni–B/TiC nano-composite deposition baths are given according to the change in particle bath concentration in Figure 3. CV graphs of pure Ni and Ni–B deposition baths are given for comparison purposes as well. While the deposition potential for pure Ni and Ni–B was around − 1.30 V during deposition, it was between − 1.30 V and − 1.42 V for nanocomposite coatings, although it varied according to the particle bath concentration values. When the graphs on the cathodic side, that is, from the positive side to the negative side, were examined, the peaks that start around 1.1 V and end around − 0.2 V show the gas output in the bath and there was no deposition in these parts of the graph. After this stage, the graph continues at the zero current level until around − 0.7 V. In this part, it is observed that no reaction occurs in the electrolyte. The sudden increase in current after the potential values around − 0.7 V indicates that the Ni metal begins to be deposited rapidly. When the CV curves of pure Ni and Ni–B alloy baths were compared with the CV curves of nanocomposite baths, it was seen that the addition of TiC particles to the bath shifts the deposition potential to the negative side and decreases the current increase rate. The addition of TiC particles affects the conductivity of the electrolyte, which in turn affects the deposition potential and the amount of deposition. This situation can be understood from the slope of the current increase rate in CV experiments. Deposition of only Ni element during storage causes an increase in current value. No current flow occurs during the deposition of B atoms and TiC particles. As seen in the CV curves, the addition of TMAB, which is a B source, to the electrolyte did not affect the current, but the addition of TiC particles caused a decrease in the current, which may be due to the fact that the particles deposited together with the Ni atoms caused a slight reduction in the amount of Ni stored.

When Ni salts are added to the electrolyte, they dissolve into Ni ions. These ions are then reduced on the substrate and deposited as Ni metal. The reduction reaction takes place as a result of the following series of reaction steps.[38,39]

$$Ni^{2+} + H_2O < \quad > Ni(OH)^{+}_{aq} + H^{+} \quad [6]$$

$$Ni(OH)^{+}_{aq} < \quad > Ni(OH)^{+}_{ads} \quad [7]$$

$$Ni(OH)^{+}_{ads} + e^{-} > NiOH \quad [8]$$

$$NiOH + H^{+} + e^{-} > Ni + H_2O \quad [9]$$

The mechanism of co-deposition of B atoms with Ni atoms as an alloy in the electrochemical coating method has not yet been fully figured out. B atoms cannot be deposited by electric current by being reduced directly from the B source added to the electrolytic bath. Instead, it is assumed to be deposited with Ni by a mechanism called the induced co-deposition mechanism. In this mechanism, instead of being stored directly in aqueous solutions, during the storage of another metal, it is deposited as an alloy with it. It is known that Ni is co-deposited as an alloy with elements such as W, Mo and P by this mechanism. The deposition event in this mechanism is different from the reduction of a single metal.[40–42] In our study, B elements added to the bath together with Ni are included in the main structure with this mechanism. Although it is not fully understood how, B atoms are detected in the analysis, and also cause changes in hardness, crystal structure, *etc.* properties. Co-deposition of reinforcing particles with the main structure metal or alloys can be explained by the Guglielmi model. In accordance with this theory, the second phase particles in the electrolyte are surrounded by a cloud of electrochemically reducible metal ions, namely,

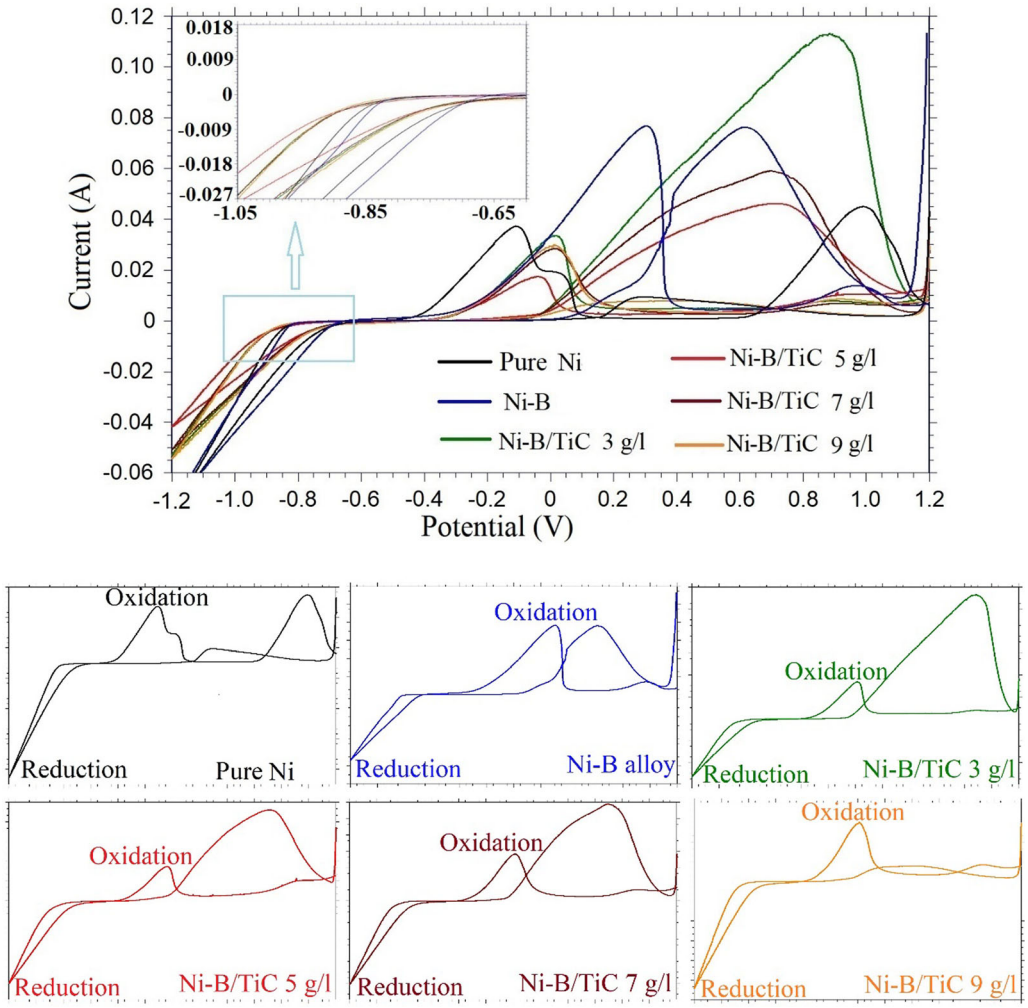

Fig. 3—CV plots of Ni–B/TiC nanocomposites, pure Ni and Ni–B alloy deposition electrolytes (presented together at the top, separately at the bottom).

metal ions are adsorbed on the reinforcement particles. Then, the particles are drawn towards the cathode (coated substrate) together with their ionic clouds with the effect of the electric current. First, the reinforcement particles are weakly adsorbed on the cathode surface. Afterthat, when the metal ions discharge their electrical charge, these particles are trapped within the gradually growing metal atoms deposited on the cathode surface, and thus co-deposition with the main structure takes place. The step-by-step co-deposition process continues in this.[40,43]

In Figure 3, when the anodic side, that is, the curve obtained when scanning from minus to plus, was examined, it was observed that there were peaks between − 0.4 V and 0.4 V values. These peaks occur due to the reverse current transition that occurs during the re-dissolution of the Ni deposited on the stainless steel and its return to the electrolyte as ions. In the CV curves, only two consecutive peaks around − 0.1 V and 0.05 V were observed for pure Ni (it may be an indication that the Ni metal was deposited in two different phases), while a single peak was observed in the curves of the other samples baths. Addition of TMAB to the bath caused the anodic dissolution peak to shift to the positive side and increase its height. With TiC particles addition to the bath, the height of the peaks decreased and shifted to the positive side. The lowest current density on both the cathodic and anodic sides was reached at 5 g/l bath concentration from the curves examined according to TiC particle concentrations. The highest particle deposition and the lowest Ni deposition are likely to be obtained at this value. In information on microhardness analysis given in Section III–D, the highest microhardnes value was measured in the sample obtained from 5 g/l TiC particle bath concentration. In addition, in the chemical content information given in Section III–C, in this sample it was observed that the particle content in the EDS results was relatively higher than the other nanocomposite samples. These results support CV graphs as well. It has been observed that the CV results obtained in general were compatible with the CV results obtained in Ni-based electrodeposition studies in the literature.[27,44]

B. *XRD Analysis of Ni–B/TiC Nanocomposite Coatings*

The XRD pattern of the TiC reinforcement particles are given in Figure 4(a). As can be seen from the

figure given, the peak at 41.8 deg (200) stands out as the strongest peak. However, the peak at 36.1 deg (111) has an intensity almost close to (200) peak. In addition to these peaks, there are peaks at 60.6 deg (220), 72.6 deg (311) and 76.4 deg (222). There are similar XRD patterns of TiC powders reflecting these peaks in the literature.[45–47]

The observation of the peaks (111) and (200) of the TiC XRD pattern given in Figure 4(a) is strong evidence of successful co-deposition of the reinforcement particles with the Ni–B main structure in the XRD patterns of the electrochemically deposited Ni–B/TiC nanocomposite coatings. Parameters obtained from the XRD pattern of TiC powders are given in Table II. The values of the peak with the highest intensity were used in the calculation of these values. The average crystal grain size of TiC powders was calculated at the level of 26.2 nm.

XRD patterns of pure Ni and Ni–B alloy coatings are given in Figures 4(b) and (c). It is seen that the peak at 51.8 deg (200) has very high intensity compared to the other peaks. In addition to the (200) peak, it was observed that specific to pure Ni the (111) peak and at low intensities the (220), (311), (222) peaks were also reflected in the XRD pattern. When the XRD pattern of the Ni–B alloy given in Figure 4(b) was evaluated, B atoms were included in the main structure of Ni and seriously affected the crystal structure of the coating with the addition of B source TMAB to the electrochemical bath. The strongest Ni -specific peak (200) has almost completely disappeared in the Ni–B alloy XRD pattern. Only the (111) peak around 44.3 deg is visible, and the intensity of this peak has decreased significantly compared to pure Ni and its width has increased. The similar XRD results are also acquired in the literature on electrodeposited pure Ni and Ni–B alloy coatings.[5,48–51]

Parameters calculated from XRD patterns of pure Ni and Ni–B alloy coatings are given in Table II. While the average crystal grain size was around 42.6 nm in pure Ni, the crystal grain size decreased significantly with its alloying with B element and was calculated as 8.7 nm. We can state that the element B transforms the main phase of Ni from a crystalline structure to an amorphous structure. At the same time, alloying with B caused an increase in microstrain and dislocation density values. It can be said that nanocrystalline Ni–B alloys are a solid solution containing B atoms in the Ni FMC structure, as the B element occupies the intermediate spaces in the Ni face-centered cubic (FMC) crystal lattice structure. Occupying interstitial spaces in the lattice structure of B atoms, which are half smaller than Ni atoms, causes tension in the crystal structure. It is possible to state that this change in the structure causes an increase in the microstrain and dislocation density values.[49]

Addition of TiC particles to the electroplating bath, the crystal structure of the Ni–B alloy mainframe was seriously affected. In Figure 5(a), XRD patterns of Ni–B/TiC nanocomposite coatings deposited at different TiC bath concentrations are given together. With the inclusion of TiC particles in the main structure, it is understood from the graphs that the peaks specific to pure Ni, which are not found in the Ni–B alloy XRD pattern, become visible again. However, while the most intense peak was (200) in pure Ni, it was clearly seen that the most intense peak in composite coating was the (111) peak of Ni. The Ni (200) peak is the second most intense peak and has higher values compared to other low-intensity peaks. It can be stated that the XRD graphs obtained are generally similar to each other with the increase in TiC bath concentration. It is seen that the Ni (111) and (200) peaks have different intensities in the form of increase or decrease with the change of TiC particle bath concentrations. However, it can be said that their densities are close to each other. In Figure 4(b), the parts of the XRD patterns between 34 deg and 56 deg are presented more closely. It is clearly seen in Figure 4(b) that the two most intense peaks (111) and (200) of TiC particles become prominent around 36 and 42 deg with the increase in TiC bath concentration. The presence of these main peaks belonging to TiC particles can be expressed as one of the most important proofs of successful co-deposition of TiC particles with Ni–B alloy.

The parameters calculated from the XRD patterns of Ni–B/TiC nanocomposite coatings and TiC particles, pure Ni and Ni–B coatings are given for comparison in Table II. The variation of mean crystal size (D), microstrain (ε) and dislocation density (δ) values calculated in XRD patterns are presented together graphically in Figure 6. It can be stated that the structure becomes more crystalline with the co-deposition of TiC particles in the main structure and consequently the rise of the XRD peaks. As can be seen in Table II and Figure 6, the increase in crystal grain size compared to Ni–B alloy also supports this situation. While the crystal grain size was calculated around 8.7 nm in Ni–B alloy, it was calculated at values ranging from ~ 9–19 nm in Ni–B/TiC nanocomposite coatings. The addition of TiC particles seems to limit the effect of B source added to the bath in reducing the crystal grain size. It can be said that nanoparticles are effective in reducing crystal grain size to a certain extent compared to pure Ni, but it is relatively limited when compared to the crystal grain size reduction that occurs as a result of alloying with B.

It was possible to state that the average crystal grain size tends to increase with the increase in TiC particle concentration in the bath as shown in Figure 6. It is seen that nanocomposite coatings exhibit a significant decrease in microstrain and dislocation density values in comparison to Ni–B alloy. The variation of microstrain and dislocation density values with the increase of TiC bath particle concentration showed an decreasing trend.

C. *Morphology and Content Analysis of Ni–B/TiC Nanocomposite Coatings*

SEM images of nanocomposite coatings, pure Ni and Ni–B alloy coatings (for comparison) are presented in Figure 7. In general, at the macro level, it can be said that the coating surfaces are flat and smooth. However, it is seen that there are differences between the specimens

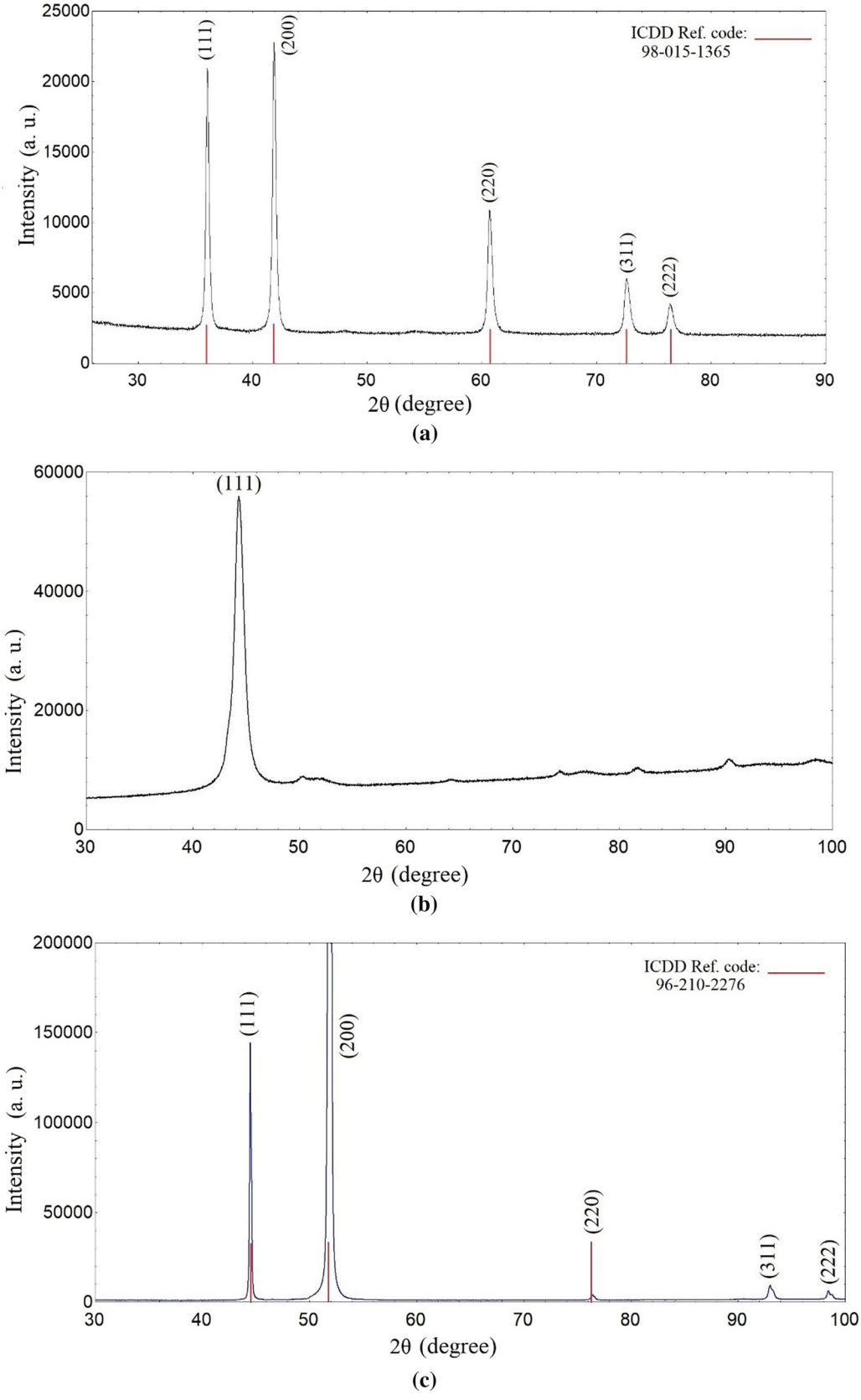

Fig. 4—XRD plot of (*a*) TiC reinforcement particles, (*b*) Ni–B alloy, (*c*) pure Ni.

Table II. Parameters Obtained from XRD Patterns of TiC Particle, Pure Ni, Ni–B Alloy and Ni–B/TiC Nanocomposite Coatings

Sample	2θ (deg)	FWHM-β (Radian)	Average Crystal Grain Size-D (nm)	Mikrostrain-ε	Dislocation Density-δ (nm^{-2})
TiC Particles	41.8	0.005910	26.2	3.86×10^{-3}	1.45×10^{-3}
Pure Ni	51.8	0.00378	42.6	1.9×10^{-3}	0.55×10^{-3}
Ni–B alloy	44.3	0.01785	8.7	10.9×10^{-3}	13.2×10^{-3}
1 g/l TiC	44.5	0.01446	10.8	8.8×10^{-3}	8.6×10^{-3}
3 g/l TiC	44	0.01186	13.2	7.3×10^{-3}	5.7×10^{-3}
5 g/l TiC	43.9	0.01680	9.3	10.4×10^{-3}	11.5×10^{-3}
7 g/l TiC	44.4	0.00928	16.8	5.7×10^{-3}	3.5×10^{-3}
9 g/l TiC	44.2	0.00945	16.5	5.8×10^{-3}	3.7×10^{-3}
12 g/l TiC	44.5	0.01003	15.6	6.1×10^{-3}	4.1×10^{-3}
15 g/l TiC	44.3	0.00847	18.5	5.2×10^{-3}	2.9×10^{-3}

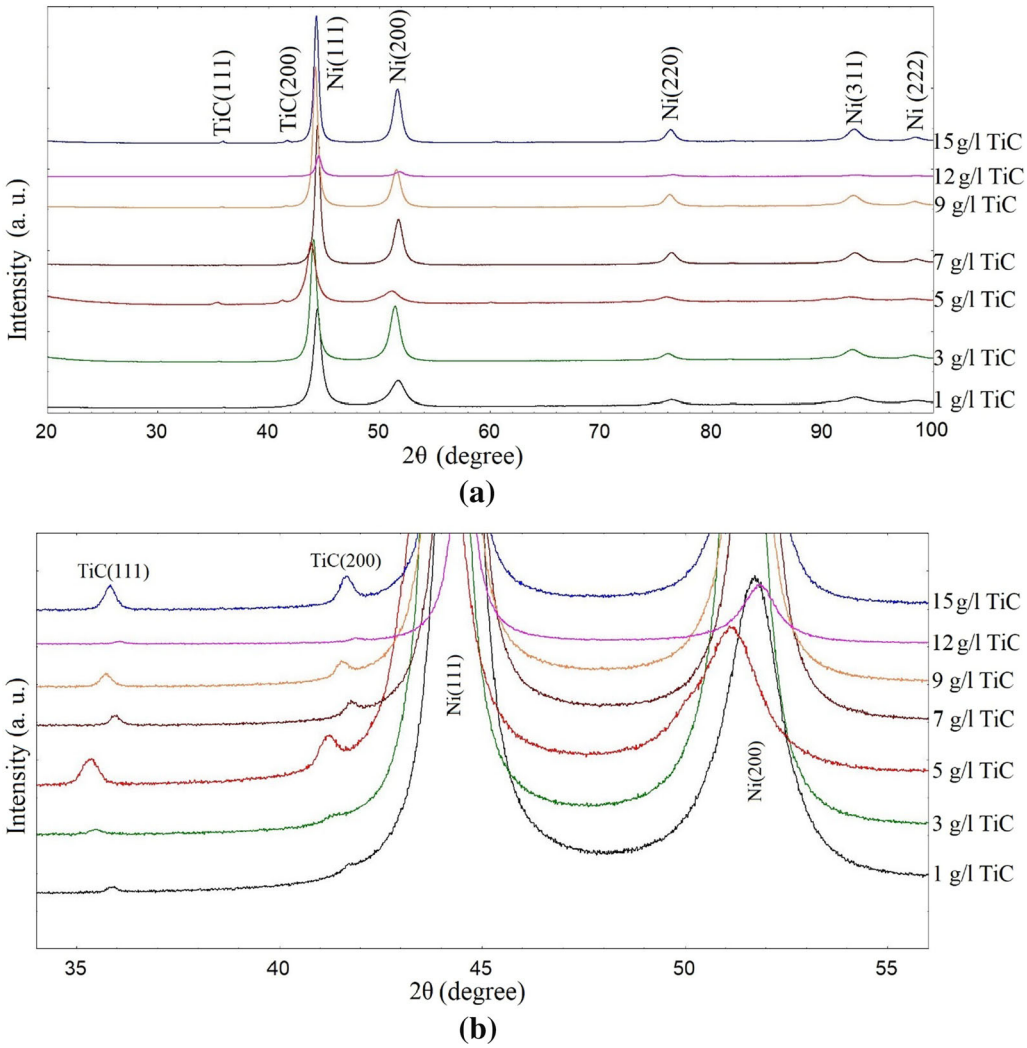

Fig. 5—XRD patterns of Ni–B/TiC nanocomposite coatings produced at different TiC bath concentrations a) XRD patterns all peaks (20-100 deg) b) TiC (111) and (200) peaks (magnified between 34-56 deg).

when the surface morphologies are examined more closely. As can be seen from the figure, it was understood that the surface structures of pure Ni, Ni–B alloy and Ni–B/TiC nanocomposite coatings were different from each other. Surface morphology in pure Ni consists of pyramidal shapes. The B source TMAB added to the bath has seriously affected the surface morphology and the pyramidal structure seen in pure Ni has completely changed, it appears as a smoother surface with circular mounds in places. With the addition of TiC particles to the bath, very serious changes were observed in the surface structure. A

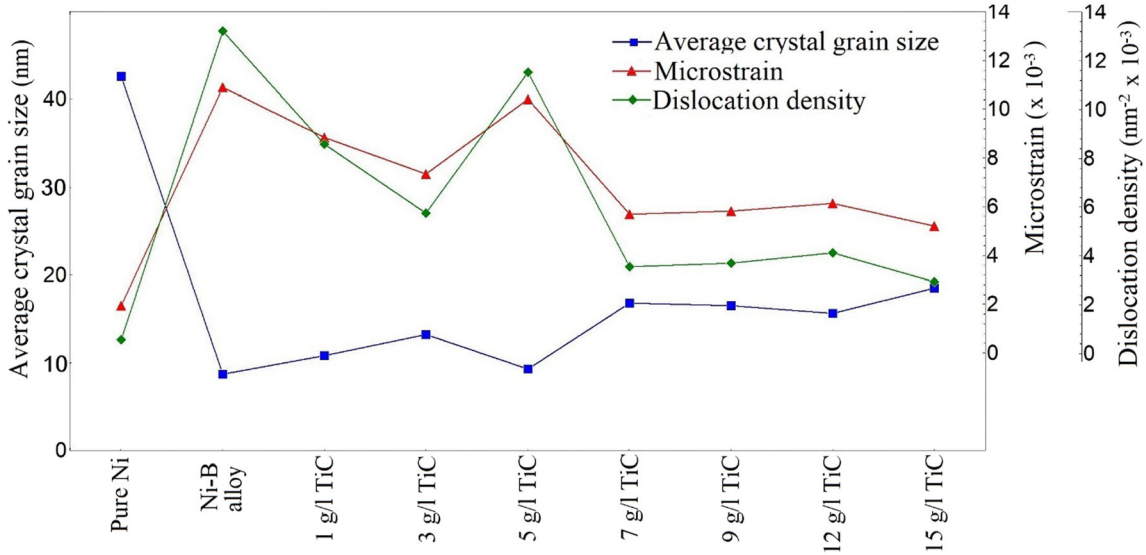

Fig. 6—Graphs of average crystal grain size (blue), microstrain (red), and dislocation density (green) (Color figure online).

cauliflower-shaped surface morphology is striking in Ni–B/TiC nanocomposite coatings. It can be reported that this type of morphology was less in the sample with 3 g/l TiC bath concentration compared to the others. In addition, it is seen that this structure resembles a bunch of grapes in images at higher magnifications. Especially in samples with 5 and 12 g/l TiC concentrations, this structure appears to be much more evident. It is thought that such an interesting structure is formed as a result of nano-sized TiC particles adhering to the substrate surface and gradually being buried in the Ni ions and B element that make up the main structure.

EDS analysis results taken from the surface of nanocomposite and Ni–B alloy coatings are given Table III. The percentage values given show the amount of element by weight.

According to the results of the analysis, it was demonstrated that the B element added to the bath for alloying and TiC particles added to the bath for reinforcement purposes were successfully deposited together with the main structure Ni. It is understood from the analysis results that the B content of nanocomposite coatings decreases with the addition of TiC particles to the electrolyte, compared to the Ni–B alloy. While the B content in the Ni–B alloy coating was 26 pct, the B content in the nanocomposite coatings was around 10 pct. Considering the Ti and C content separately and the total TiC content in nanocomposite coatings, there is no regular increase or decrease trend with the increase in the particle content in the bath. In the sample with 5 g/l TiC bath concentration, the TiC content increased compared to the sample with 3 g/l TiC, then with the increase in the particle content in the bath, the particle ratio in the coating also showed a decreasing trend. Afterwards, the particle ratio in the coating tended to decrease again in the sample with 15 g/l TiC, after a limited increase in the sample with 12 g/l TiC bath concentration. In the morphology of the samples with a higher particle content of 5 and 12 g/l, It can be observed that they have a different structure compared to the other samples. The structure consisting of cauliflower-shaped grape bunch-like and circular-shaped heaps is more noticeable in these samples. In this case, it can be noted that the morphology changed in this way with the increase in TiC content in the coating.

Element mapping images of nanocomposite sample with 5 TiC bath concentrations, which have relatively higher TiC content according to the results of EDS analysis, are given in Figure 8. As can be seen in the mapping image, it was understood that the alloying element B and the reinforcement particle TiC ceramics distribute homogeneously within the main structure and were successfully co-deposited with the main structure.

Cross-sectional SEM images of nanocomposite coatings and pure Ni are shown in Figure 9. From the figure, it is appeared that some of the coatings are separated from the substrate material, and in some of them, although they are not completely separated from the substrate, a clear distinction can be made from the substrate in the form of a line. The vibrations and forces that occur during the cutting of the samples may cause some separation of the coating material from the substrate. Furthermore, there are parts where the coatings adhere well to the substrate material. It can be seen that the coatings with 3 and 12 g/l TiC bath concentrations and the pure Ni coating adhere well to the substrate material. While the coating thickness was measured around 50–60 μm in pure Ni, coating thicknesses in nanocomposite coatings were measured around 15–20 μm in most of the samples. Only in the sample with a TiC particle bath concentration of 5 g/l, the thickness was measured around 10 μm. Since the Ni–B alloy could not adhere to the substrate due to internal tensions, it was not possible to obtain the cross-sectional image. However, the coating thickness was measured with a micrometer and it was found to be around 40–45 μm.

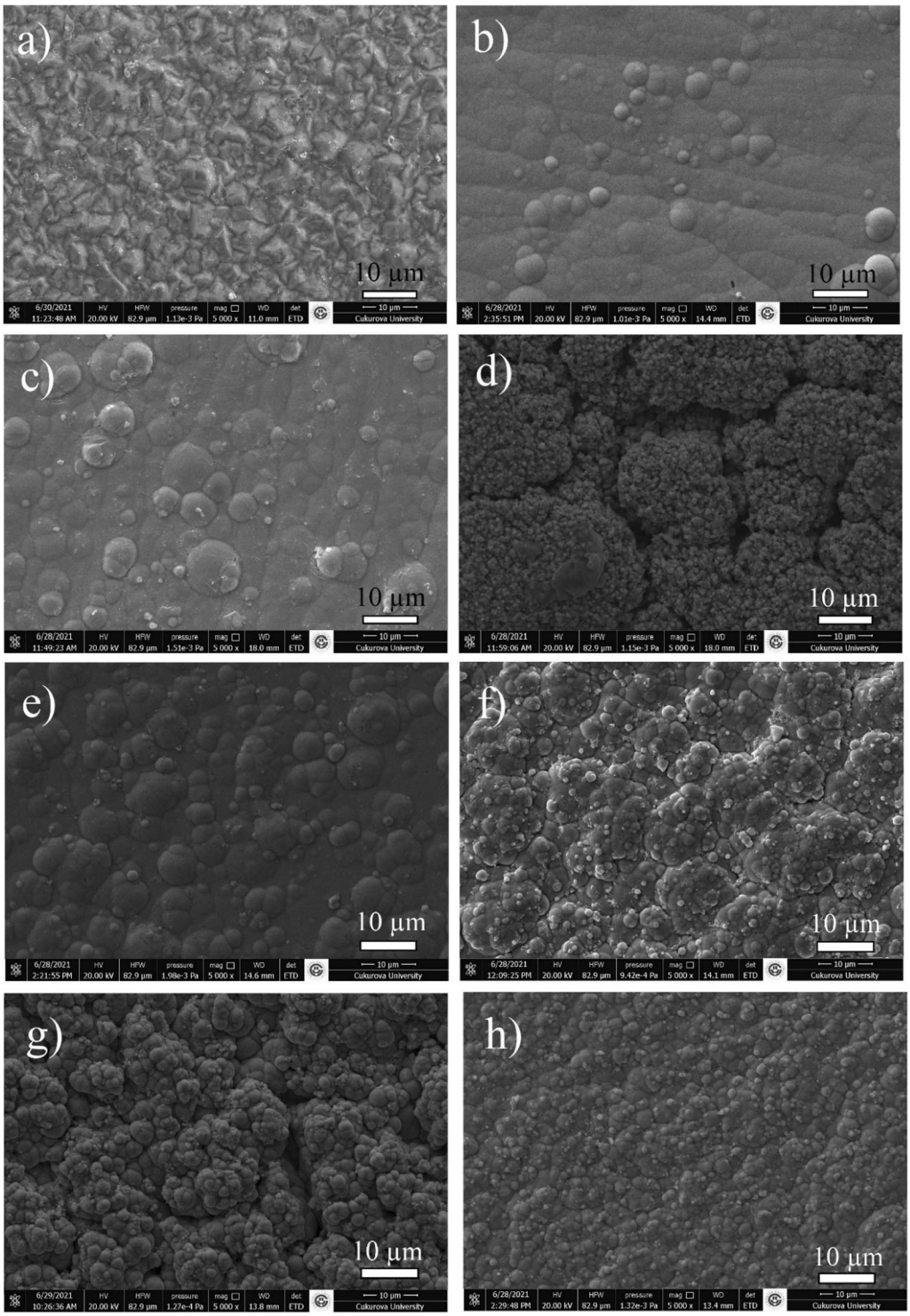

Fig. 7—SEM images of the coatings at 5000 × magnification, (*a*) pure Ni, (*b*) Ni–B alloy and (*c*) 3 g/l, (*d*) 5 g/l, (*e*) 7 g/l, (*f*) 9 g/l, (*g*) 12 g /l, (*h*) 15 g/l TiC bath concentration Ni–B/TiC nanocomposite coatings.

When the thickness information of the coatings was examined, the addition of TMAB to the bath caused a decrease of around 10 pct in the coating thickness, and in this case, it was understood that the alloying with B causes a decrease in the current efficiency when compared to the pure Ni bath. In addition, the decrease in current efficiency seen with the decrease in coating thickness with TiC reinforcement was much higher, and it was seen that the coating thicknesses were reduced by more than 50 pct compared to pure Ni.

Elemental mapping analyzes obtained from cross-sectional images of Ni–B/TiC nanocomposite coatings produced in electrolyte with 5 and 12 g/l TiC bath concentrations are presented in Figures 10(a) and (b). The mapping analyzes clearly showed that the TiC ceramic particles were homogeneously distributed throughout the entire cross section and were included in the main structure of the coating.

D. *Microhardness Analysis of Ni–B/TiC Nanocomposite Coatings*

In Figure 12, the microhardness values of the deposited Ni–B/TiC nanocomposite coatings are given according to the particle bath concentration change. The microhardness values of the stainless steel substrate and pure Ni and Ni–B alloy coatings were given in the same figure so as to make a comparison. According to the measurements, the microhardness values were obtained as 203 HV for stainless steel, 290 HV for pure Ni, and 400 HV for Ni–B alloy. It was appeared that the pure Ni plating was approximately 45 pct harder than stainless steel. TMAB addition to the deposition bath, the hardness value increased by approximately 38 pct compared to pure Ni as a result of alloying pure Ni with B. Sheu *et al*.[52] studied the hardening mechanism for electrodeposited Ni–B alloys and reported that the increase in hardness was owing to solid solution hardening and grain size reduction.[30–37,52,53] In the examination of Figure 11, it is seen that the hardness value first increases and then decreases with the increment in particle bath concentration. The highest microhardness value was obtained at 5 g/l TiC particle concentration. At this concentration, the hardness increased approximately 160 pct compared to pure Ni and approximately 90 pct compared to Ni–B alloy coating. Similarly, increases in microhardness were obtained in studies in the literature where Ni–B alloy was reinforced with particles such as TiO_2, Al_2O_3, TiN, B_4C, Si_3N_4.[1,11,16,54,55] At bath concentrations higher than 5 g/l, it is possible to experience some decrease in hardness as a result of possible aggregation problems of TiC particles increasing in the electrolyte and therefore structural irregularities that may occur in the coating layers that grow during deposition. According to the results of the EDS analyzes given in Table II of Chapter 3.3, the TiC particle content obtained in the coating at concentrations greater than 5 g/l tends to be relatively low. In this case, even if the particle content in the bath increases, it is seen that this increase is not reflected in the coating particle content as a result of possible agglomeration, *etc*. problems. Similar situations can be seen in other electrodeposition systems in the literature.[51,56]

The increase in hardness with particle reinforcement to the Ni–B alloy is explained by the Orowan dispersion-hardening mechanism in the literature. The availability of hard particles in the structure prevents the dislocation movements and the dislocation pinning effect of the dispersed particles causes a strength-enhancing effect.[40]

E. *Corrosion Analysis of Ni–B/TiC Nanocomposite Coatings*

1. *Open circuit potential analysis of Ni–B/TiC nanocomposite coatings*

OCP curves of Ni–B/TiC nanocomposite coatings and OCP curves of stainless steel substrate, pure Ni and Ni–B alloy coatings are given in Figure 12. OCP results represents the oxidation and reduction activities for the solution medium. It can be stated that the samples whose OCP curves are on the more positive side are more resistant to corrosion.[57,58]

As shown in Figure 12, the steel substrate is more corrosion resistant when coated with either pure Ni or Ni–B alloy. The stable corrosion resistance of pure Ni plating can be seen from the figure. Although Ni–B alloy initially seems more corrosion resistant than Ni plating, its potential decreases to more negative values over time. It can be said that this situation is caused by the continuous increase in corrosion activities due to fractures and cracks in the main structure of the Ni–B alloy due to internal stresses. Bekish *et al*.[49] reported that the corrosion resistance decreases with the increase of B content in Ni–B alloy coatings and that corrosion processes may accelerate due to the formation of very small galvanic pairs between the crystalline and amorphous phases in such heterogeneous coatings. The authors also reported that with an increase in B content, corrosion protection decreases due to an increase in defect and looseness.[49] In addition, the OCP potential of the stainless steel substrate was more negative than the other samples.

With the reinforcement of the Ni–B alloy with TiC particles, the OCP curves shifted to the more positive side compared to pure Ni. The tendency of the OCP curves of the nanocomposite coatings to shift to the positive side continued with the increase of TiC particle concentrations added to the bath. In this case, it is seen that the reinforcement TiC particles improve the corrosion resistance. At the end of 3600 s, the OCP potential was measured as -0.584 V in pure Ni and -0.476 V in the nanocomposite coating produced in the bath with 12 g/l TiC particle concentration. The improvement in corrosion resistance with the inclusion of TiC particles in the structure can be attributed to the reduction of the active areas of the Ni–B alloy main structure due to the reinforcement particles. Similar improvements in corrosion performance were also observed in reinforcement particles such as Fe_2O_3, AlN, hBN, YSZ, which were previously co-deposited with Ni–B alloy.[17,44,59,60]

2. *Corrosion analysis of Ni–B/TiC nanocomposite coatings by potentiodynamic polarization method*

Tafel curves of Ni–B/TiC nanocomposite, pure Ni, Ni–B alloy coatings and stainless steel substrate are given in Figure 13. Corrosion potential (E_{cor}), corrosion current (I_{cor}) and corrosion rate data obtained from these curves are presented in Figure 14.

From the examining of the results obtained from Figures 13 and 14, it is seen that the TiC particle reinforcement is extremely effective in terms of corrosion protection. While the corrosion current values were

Table III. EDS Content Analysis of Coatings

Sample	Nickel (Ni)	Boron (B)	Titanium (Ti)	Carbon (C)	TiC (Sum of Ti ve C)
Ni–B Alloy	73.4	26.6	—	—	—
3 g/l TiC	79.01	9.97	0.5	10.53	11.03
5 g/l TiC	66.34	12.52	2.28	18.85	21.13
7 g/l TiC	76.53	13.85	0.61	9	9.61
9 g/l TiC	82.29	11.56	0.48	5.67	6.15
12 g/l TiC	77.37	11.87	2.42	8.34	10.76
15 g/l TiC	82.49	11.86	0.52	5.13	5.65

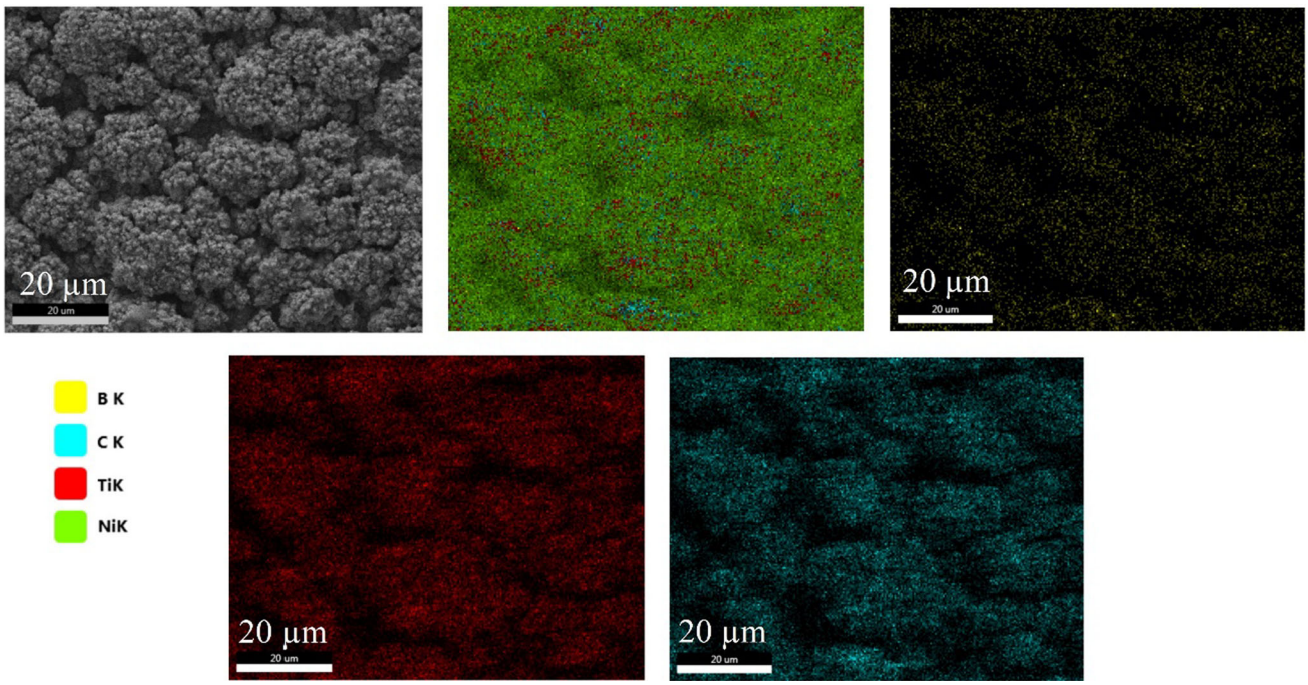

Fig. 8—Surface EDS mapping analysis of nanocomposite coating with 5 g/l TiC bath concentration.

calculated as 10.5×10^{-5} A and 12.47×10^{-5} A in pure Ni and Ni–B coatings, this value decreased significantly in nanocomposite coatings and was calculated between 2.83×10^{-5} and 4.75×10^{-5} A. According to the Tafel data, although the corrosion resistance performances of pure Ni and Ni–B alloy coatings seem to be close to each other, the performance of the Ni–B alloy coating was slightly lower. In addition, the corrosion performance results of the stainless steel substrate appear to be very close to pure Ni in terms of corrosion current and corrosion rate, while the corrosion potential value was quite negative from both pure Ni and Ni–B alloy, in line with the OCP results. In terms of corrosion current and corrosion rate, the corrosion performance of stainless steel was slightly lower than that of pure Ni and higher than that of Ni–B alloy.

When nanocomposite coatings were evaluated within themselves, it was noticed that the best data in terms of corrosion resistance were obtained in the coating sample produced in a bath with a 12 g/l TiC bath concentration. The sample with 6 g/l TiC bath concentration was observed as the sample with the lowest corrosion performance. If the sample with 3 g/l TiC bath concentration was ignored, it was seen that the corrosion resistance increases with the increase in TiC concentration, but these increases cannot be said to be very serious increases. In other words, the corrosion performances of nanocomposite samples seem to be close to each other in terms of corrosion current and corrosion rate. Even the lowest corrosion performance of nanocomposite coatings was much better when compared to pure Ni and Ni–B alloy coatings. The sample with 12 g/l TiC concentration in the best condition performed 371 pct better than pure Ni and 440 pct better than Ni–B alloy in terms of corrosion current. Namely, the sample with 12 g/l TiC concentration showed 73 pct lower corrosion rate than pure Ni and 77 pct lower than Ni–B alloy in terms of corrosion rate. In terms of corrosion potential, samples with 9 and 12 g/l TiC bath concentrations seem to be in much better condition than pure Ni and Ni–B coatings, while samples with 3 and 6 g/l TiC bath concentrations seem to be very close to pure Ni. However, in the interpretation of Tafel data, the corrosion potential alone does not reveal a sufficient

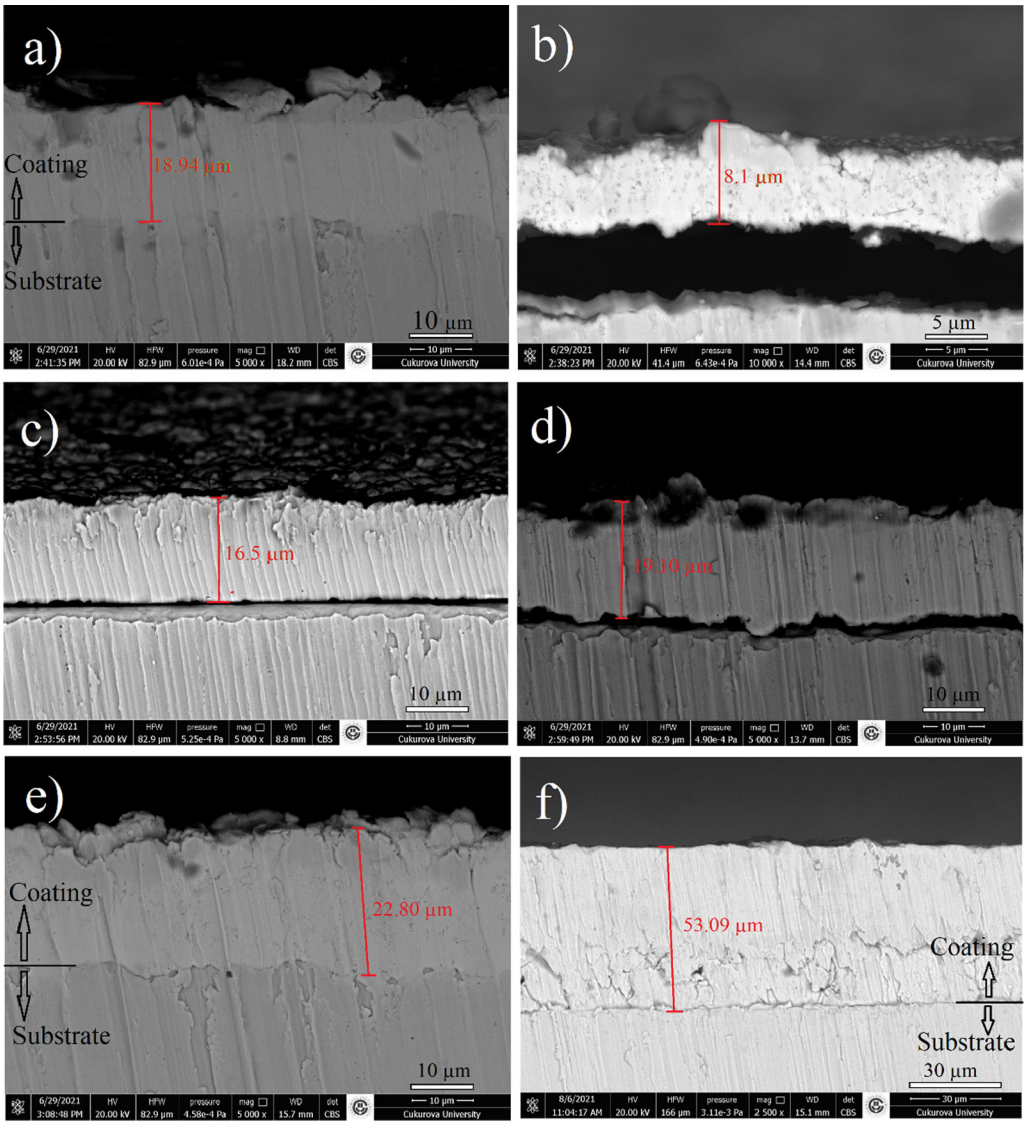

Fig. 9—Cross-sectional images of Ni–B/TiC nanocomposite coatings, (*a*) 3 g/l TiC, (*b*) 5 g/l TiC, (*c*) 7 g/l TiC, (*d*) 9 g/l TiC, (*e*) 12 g/l samples with TiC bath concentrations, f) pure Ni.

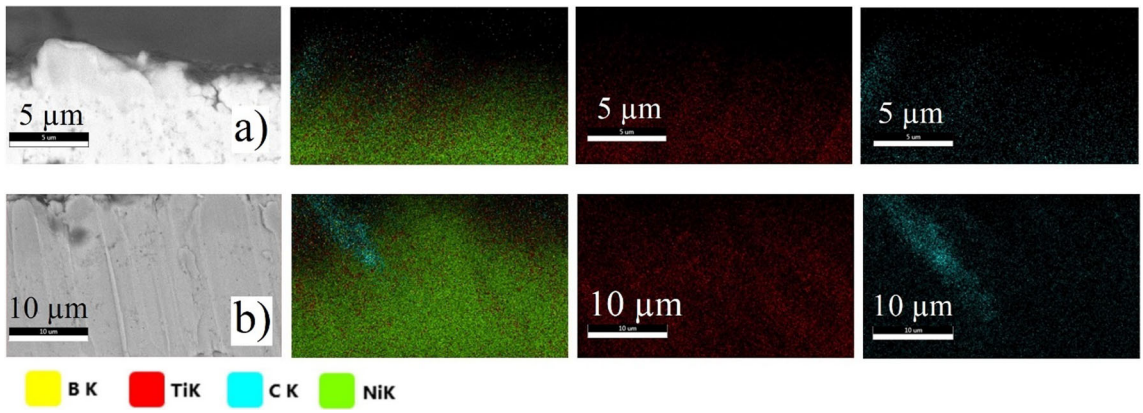

Fig. 10—Elementel mapping EDS analysis on Ni–B/TiC nanocomposites cross-section with(*a*) 5 g/l, (*b*) 12 g/l TiC concentration mapping EDS.

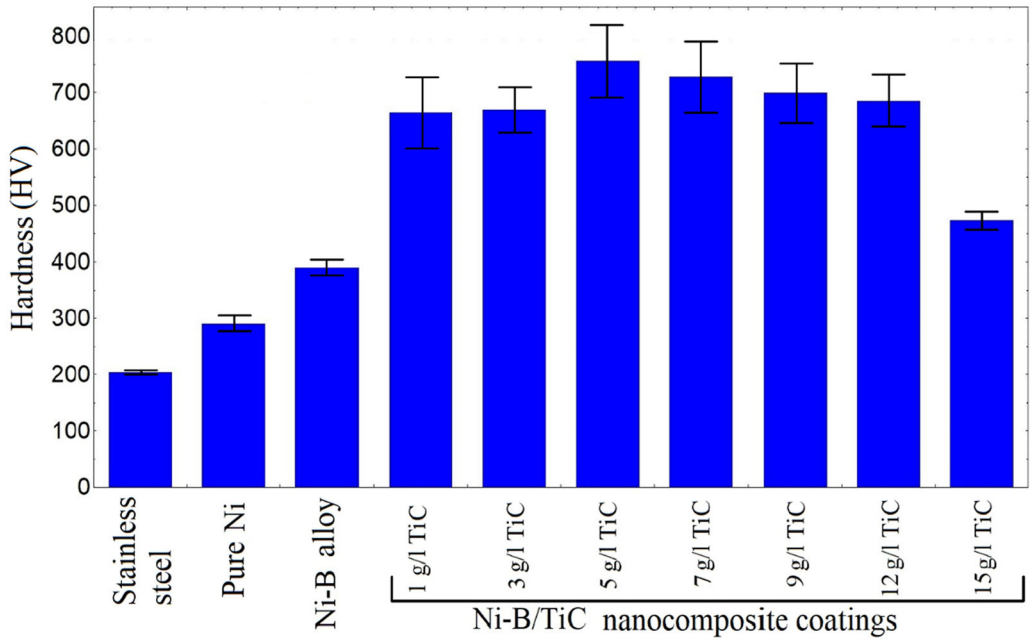

Fig. 11—Microhardness values of stainless steel substrate, pure Ni, Ni–B alloy and Ni–B/TiC nano-composite coatings.

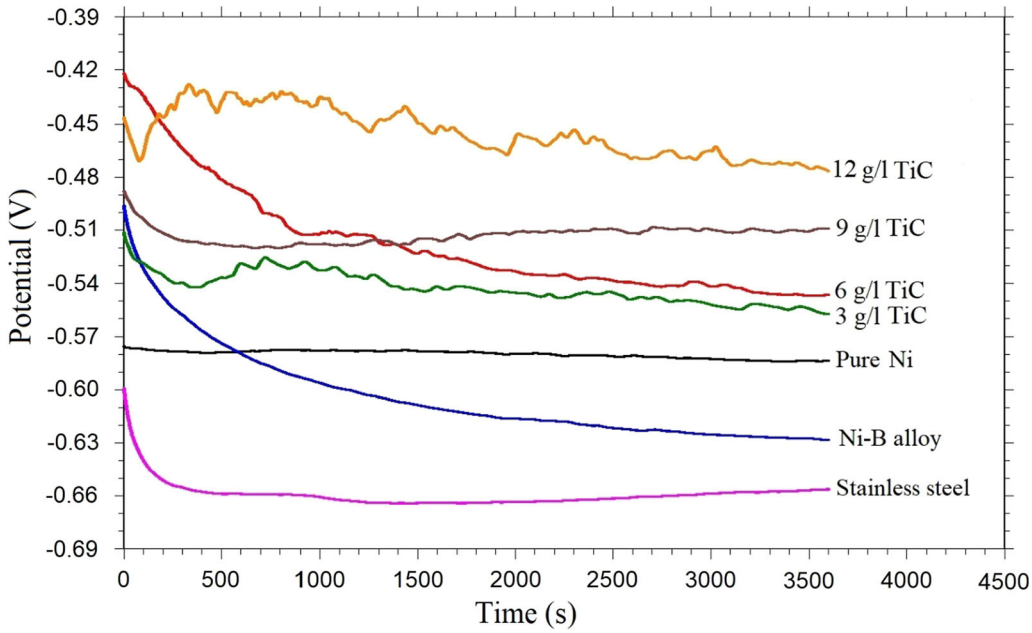

Fig. 12—OCP curves of Ni–B/TiC nanocomposite coatings and stainless steel substrate, pure Ni and Ni–B alloy coatings.

result, and it should be evaluated together with the corrosion current and corrosion rate. It was understood that supporting the Ni–B alloy main structure with TiC reinforcement particles was very effective in terms of corrosion resistance evaluating the all the data.

This promotion in corrosion resistance was explained by various opinions in the literature. It can be argued that it is due to the fact that the cracks, voids and micron-sized holes on the surface of the composite coating were filled by TiC particles and act as a physical barrier. The addition of the reinforcement second phase particles to the main structure acts as a blocker in terms of hydrogen formation reactions on the coating surface, that is, the reinforcement particles cause the active areas on the coating surface to decrease. The availability of reinforcement TiC particles in the Ni–B mainframe affects the kinetics of both cathodic and anodic electrochemical reactions, that is, suppresses the cathodic and anodic reaction processes. In addition to cathodic hydrogen formation reactions, anodic dissolution reactions are also seriously affected by this situation.[61] Moreover, the addition of boron and TiC to the Ni main

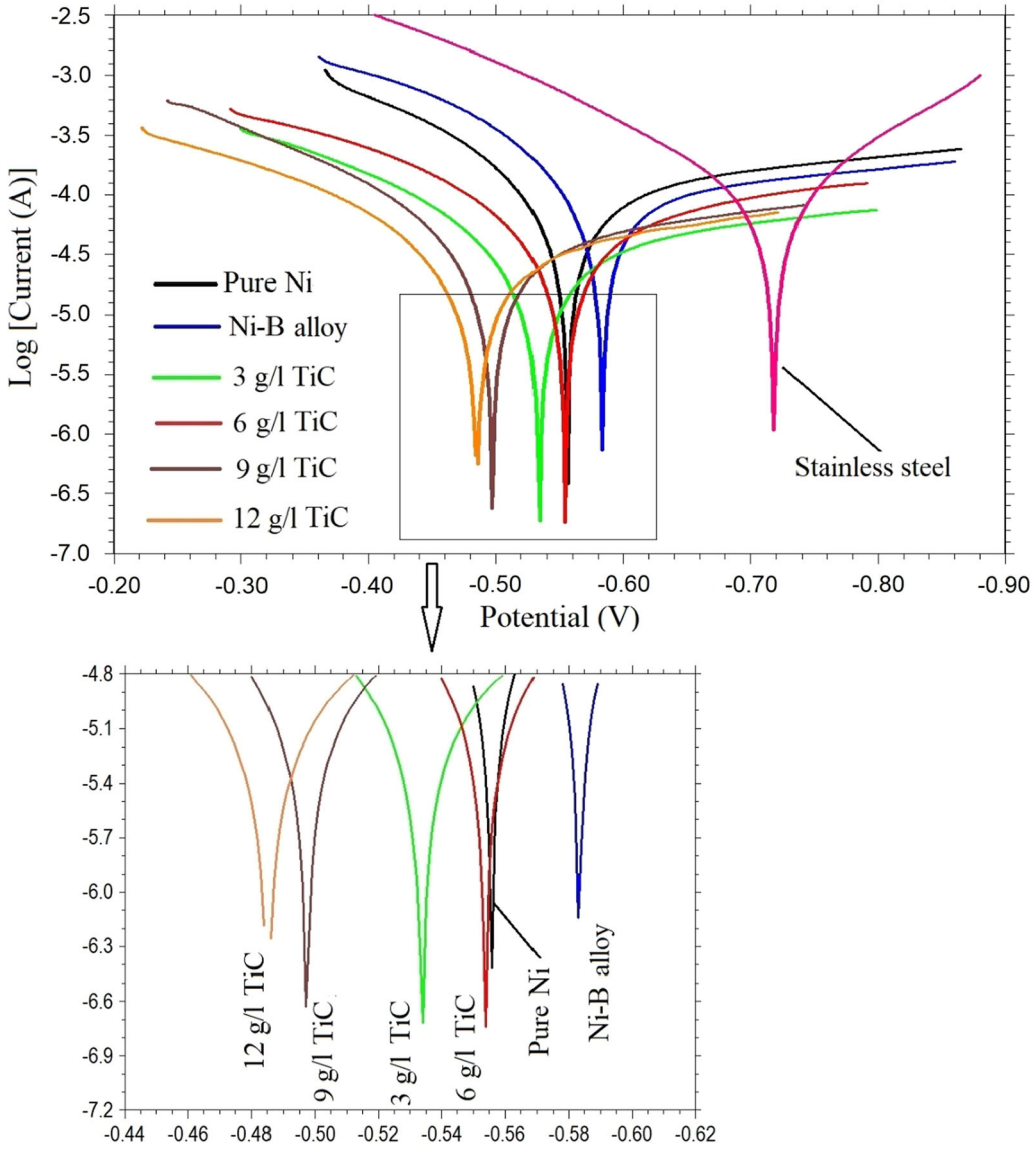

Fig. 13—Tafel curves of Ni–B/TiC nanocomposite, pure Ni, Ni–B alloy coatings and stainless steel substrate.

structure causes a decrease in crystal grain size, and the improvement of corrosion resistance can be associated with a decrease in crystal grain size. Because fine-grained materials have a denser structure, it is expected that they are more resistant to corrosion.[62,63] Another view regarding the increase in corrosion resistance is that the reinforcement particles, which are well distributed at the grain boundaries during the electrochemical coating operation, reduce the faults in the coating and make the coating more compact and less pervious. This situation causes an increase in corrosion resistance.[51]

F. *Wear Analysis of Ni–B/TiC Nanocomposite Coatings*

Wear analysis could be performed for pure Ni and Ni–B/TiC nanocomposite coatings, but wear analysis could not be performed for Ni–B coatings because the coating could not adhere to the substrate due to excessive internal stress. A stable ground could not be obtained due to cracks, flaking, spalling and curling in all Ni–B alloy sample coatings obtained as a result of various trials. In previous microhardness measurements, it was stated that the hardness values of Ni–B/TiC nanocomposite coatings were higher than those of pure Ni and Ni–B alloy coatings. With the increase in hardness values, an improvement in wear resistance is also a predictable situation. In Figure 15, the friction coefficient graphs of pure Ni and Ni–B/TiC nanocomposite coatings are presented together. Furthermore, the average values of the coefficient of friction obtained from the coatings are given in Table IV. When the curves in Figure 15 were examined, it was indicated that the friction coefficient values of Ni–B/TiC nanocomposite coatings produced at 3, 7 and 12 g/l TiC bath concentrations were at lower values compared to pure Ni. It was understood that the average friction coefficient values of nanocomposites given in Table IV were quite low compared to pure Ni. It can be stated that the

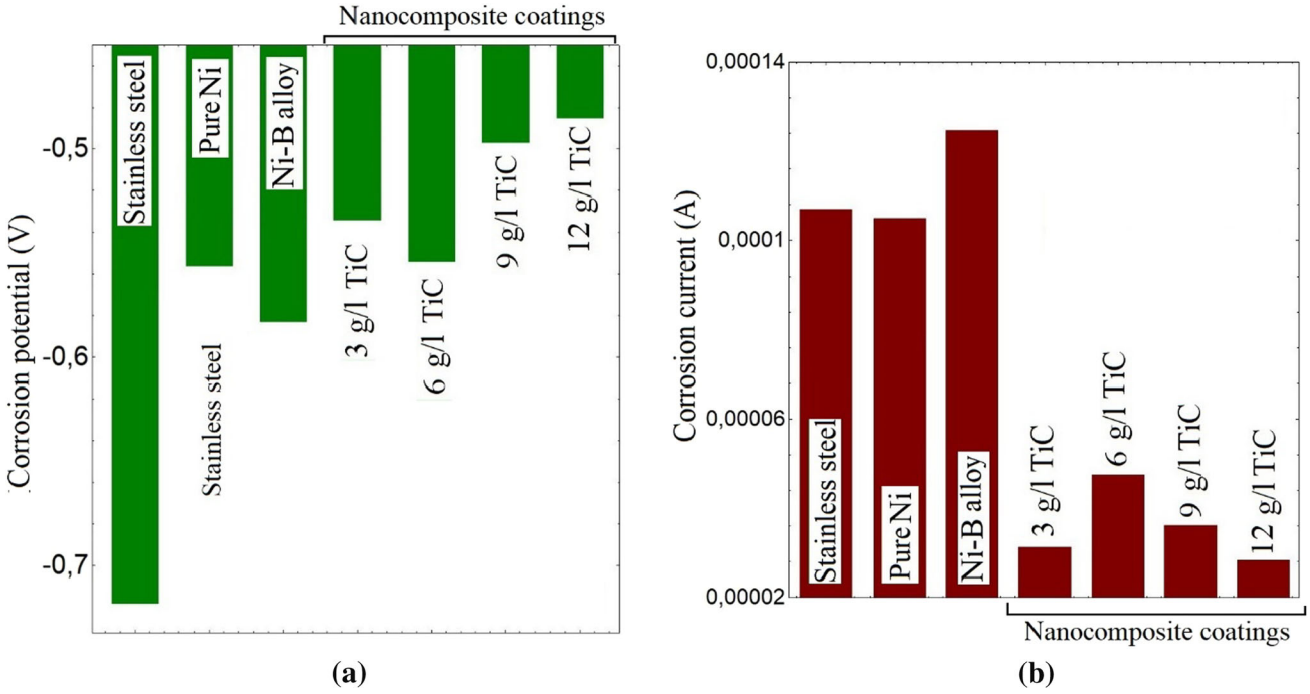

Fig. 14—(*a*) Corrosion potentials, (*b*) corrosion curtent of Ni–B/TiC nanocomposite, pure Ni, Ni–B alloy coatings and stainless steel substrate.

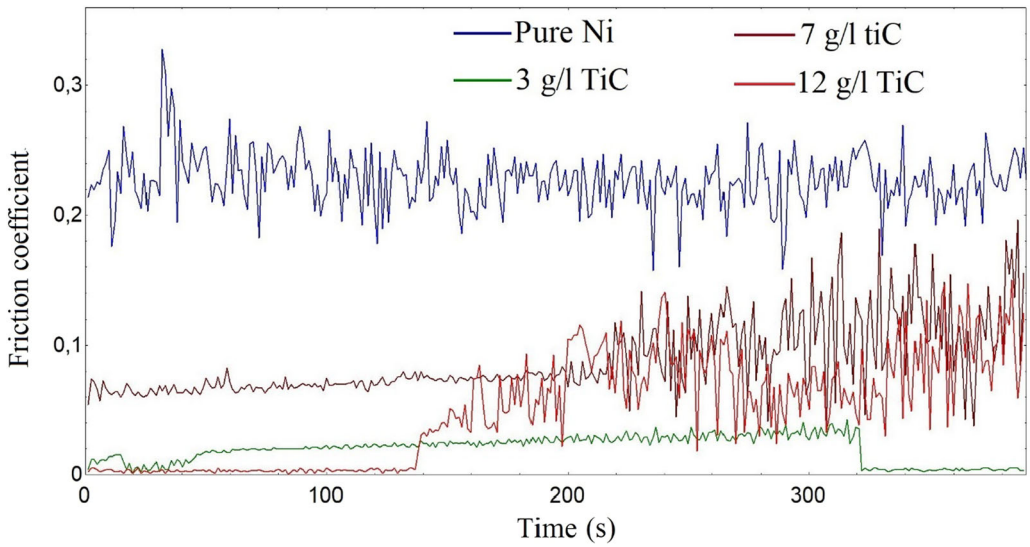

Fig. 15—Friction coefficient graphs of pure Ni and Ni–B/TiC nanocomposite coatings.

friction coefficient values may have decreased compared to pure Ni due to the increased hardness as a result of both B alloying and TiC particle reinforcement, as well as the contribution of nano carbide particles in the main structure.[27,64] It was seen that the friction coefficient curves in the figure follow an oscillating course in the form of continuous increases and decreases. It is striking that the amplitude of the oscillation appearance was higher in this way, especially during the whole test period in pure Ni and after a certain period of the test in nanocomposite coatings. This high oscillating course in the coefficient of friction graphs gives the impression that wear occurs by sticking and sliding movements. During adhesion, the friction coefficient first increases up to a certain maximum value, followed by a sudden decrease in the friction coefficient with rupture.[64,65] When the friction coefficient curves of nanocomposite coatings with 7 and 12 g/l TiC bath concentrations were examined more closely, it was proved that the friction coefficient values progressed at lower values at the beginning of the wear test and the friction coefficient values increased after certain values. It can be argued that this situation may have occurred as a result of the breaking of the slippery layers that may have dominated

Table IV. Average Friction Coefficient, Wear Volume Loss, Microhardness and Surface Roughness Values of Pure Ni and Ni–B/TiC Nanocomposite Coatings

Sample	Average Friction Coefficient	Wear Volume Loss (mm^3)	Mikrohardness (HV)	Average Crystal Grain Size (nm)	Surface Roughness (μm)	
					Ra	Rz
Pure Ni	0.227	0.017212	290	42.6	0.1247	0.5121
3 g/l TiC	0.0196	0.004104	670	13.2	0.1324	0.6472
7 g/l TiC	0.0876	0.002933	727	16.8	0.1445	0.9126
12 g/l TiC	0.0491	0.001795	685	15.6	0.2037	1.35

the surface at first, along with the progress of the abrasion test.

The wear volume loss values, the hardness, average crystal grain size and surface roughness values of the samples are given in Table IV.

From the examination of the wear volume loss datas given in Table IV, it is seen that the wear loss decreases with the increase in TiC bath concentration, unlike the change in friction coefficient values. However, it can be stated that the wear volume loss values in all nanocomposite coatings were quite low compared to pure Ni and were generally close to each other. For example, in nanocomposite coating with 3 g/l TiC bath concentration, it can be stated that the wear volume loss was reduced by 93 pct compared to pure Ni. As mentioned before, increased hardness and changing main structure as a result of alloying with B and supporting with TiC particles were very important factors in reducing the wear volume loss.[27,66] The lowest abrasion volume loss was obtained in the sample with 12 g/l TiC bath concentration. Considering the hardness values in Table IV, the fact that the highest hardness value belongs to the sample with 7 g/l TiC, while the lowest wear volume value belongs to the sample with 12 g/l TiC shows that the increase in TiC content affects the wear behavior. Although the hardness values of the samples with 3 g/l and 12 g/l TiC bath concentrations were close to each other, it was observed that there were differences in the wear performance values. In this case, it can be stated that the change in the particle content in the main structure due to the difference in TiC bath concentration between the two samples and the morphology differences affected the wear mechanism as seen in SEM images. It can be argued that the cauliflower-like appearance has a positive contribution to the wear performance, especially in the nanocomposite sample with 12 g/l TiC. When the wear resistance of the samples is evaluated over the crystal grain sizes given in Table IV, it is seen that the grain sizes of nanocomposite coatings are much lower than pure Ni. Decreasing grain size and increasing microstrain and dislocation density values (Figure 6) cause an increase in material strength and hardness, and in this case, it has an improving effect in terms of wear resistance.[63,67] Although the crystal grain size values showed a slight increase with the increase in TiC bath content, it is seen that the values are quite close to each other. In the literature, it is stated in the detailed wear behavior analyzes of Ni-based electrodeposited materials that the crystal grain size reduction up to a certain value improves the wear behavior.[68,69] When the surface roughness values given in Table IV were examined, it was seen that the surface roughness values of nanocomposite coatings are relatively higher than pure Ni, and it was observed that the surface roughness values increase with the increase in the amount of particles in the bath. When evaluated together with the wear data, it was seen that the increase in roughness resulting from the particle reinforcement contributes positively to the wear behavior.

Wear trace surface SEM images of pure Ni and nanocomposite coatings are presented at different magnifications according to the trace condition in Figure 16. Although the nanocomposite sample with 3 g/l TiC bath concentration appears closer to pure Ni in terms of surface morphology, it is a material with considerably higher hardness than pure Ni. As can be seen in Figure 15, the lowest friction coefficient curve was observed in the sample with 3 g/l TiC bath concentration. However, it was seen that the friction coefficient in the samples with 7 and 12 g/l TiC bath concentrations increased compared to the sample with 3 g/l TiC. In this case, it can be thought that the different surface morphologies of the samples with 7 and 12 g/l TiC bath concentrations affect the friction coefficient. Because the surface of these nanocomposite samples has a cauliflower-like shape. It can be argued that the wear behavior on a surface consisting of large and small micro-peaks may also be affected differently than on a flatter surface.

The wear trace SEM images of pure Ni are given in Figure 16(a), it is seen that plastic deformation was observed in general and the adhesion wear mechanism was dominant. High local tensile and compressive stresses under cyclic loading are the cause of plastic deformation that come about in the roughness of articulated surfaces. As the roughness sticks, a local connection is formed between them and then it starts to break at its weakest point. This broken material is transferred to the hinged surfaces and therefore can cause surface friction. Moreover, strain hardening may occur on surfaces exposed to repeated loads, which may lead to the formation of a delamination type wear mechanism owing to increase in surface hardness.[27] The contrast change in the form of darkening seen in the wear trace gives the impression that there may be hardening and oxidation in the wear area as a result of the heat arising from friction.[11,27,29,70–73] The O content of approximately 10–12 pct in the EDS analyzes taken

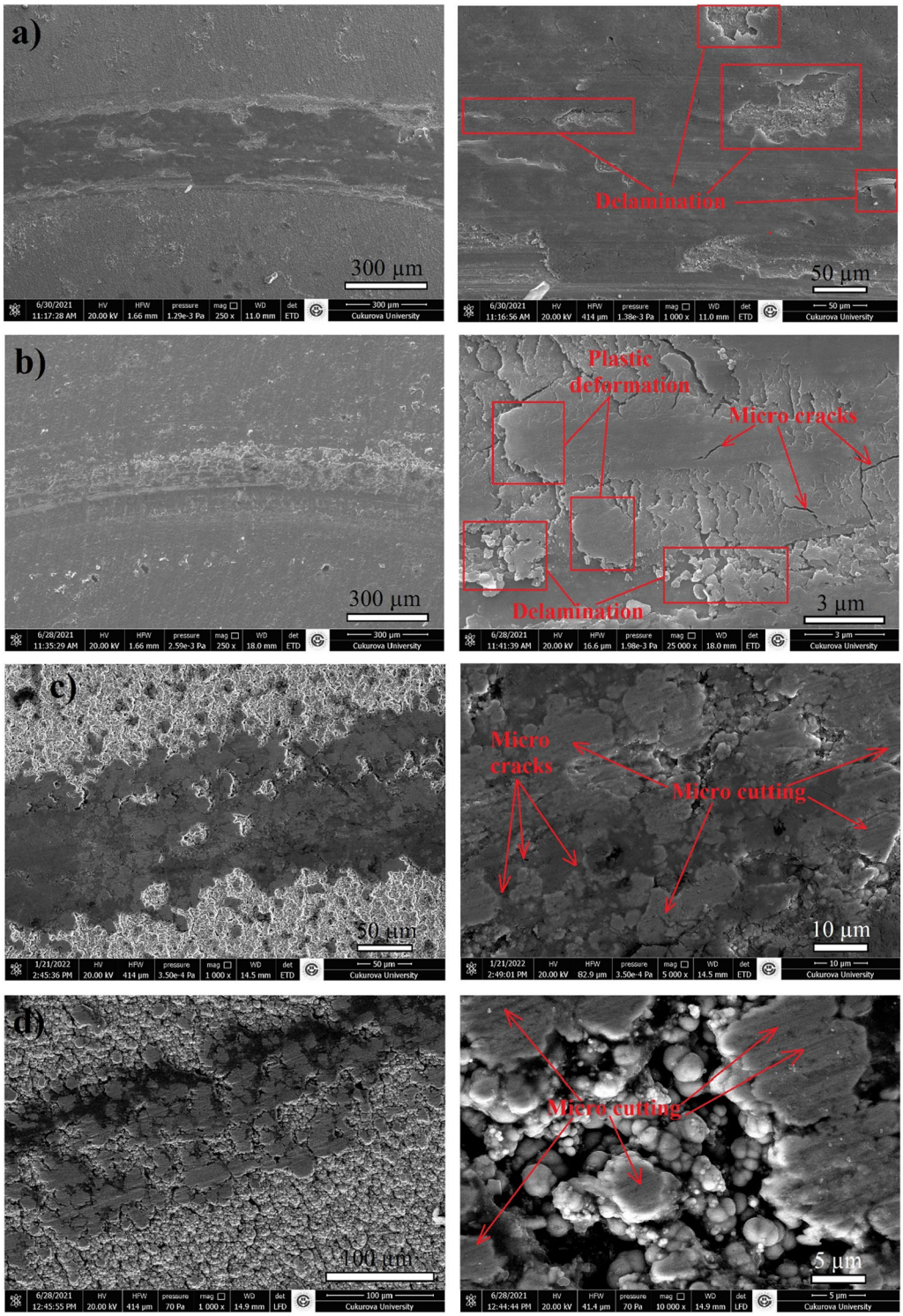

Fig. 16—Wear track SEM images (*a*) Pure Ni coating, (*b*) 3 g/l TiC, (*c*) 7 g/l TiC, (*d*) 12 g/l TiC bath concentrations Ni–B/TiC nanocomposite coaitngs.

from the wear trace of pure Ni supports this view. Signs of delamination type wear were observed when examined the wear trace SEM images of pure Ni at 1000 magnification. In delamination or fatigue-type wear, subsurface cracks may coalesce as net and cause damage due to exposure to loads acting on the surface. Fatigue-induced delamination type wear results from subsurface deformation leading to nucleation of voids and cracks followed by crack propagation parallel to the surface. As a result, crack propagation occurs towards the surface and wear layers are formed. Crack formation and propagation are due to repeated and

alternating mechanical stresses below the contact surface.[74–76]

Wear trace SEM images of Ni–B/TiC nanocomposite coating deposited at 3 g/l TiC bath concentration are given in Figure 16(b). It was seen that there was a much shallower wear trace when compared to pure Ni. It was especially noticeable that there were still intact parts on the surface. With increasing hardness and TiC reinforcement, it is expected that the wear will remain more superficial. In general, it can be clearly seen in the high magnification SEM image where plastic deformation was dominant in the wear mechanism. In addition, cracks were seen in the deformed layers in the SEM image and it was noticed that there was a delamination type wear.[28] No clear signs of abrasive wear were found in this nanocomposite material, which has a very high hardness compared to pure Ni. For this reason, it can be thought that the micro-particles that were broken off during the abrasion test may have adhered to the surface or may have quickly moved away from the environment.

In Figure 16(c), wear trace SEM images of Ni–B/TiC nanocomposite coating deposited at 7 g/l TiC particle bath concentration are presented at different magnifications. In general, it can be stated that the wear mechanism was abrasive. In particular, the presence of micro scratches at high magnification indicates that the micro-cutting wear mechanism was dominant.[72] The presence of darker areas in the wear trace is striking. In darker areas, it can be stated that oxidation may have occurred with high heat caused by friction.[11,27,29,70–73] In the EDS analyzes taken from these areas in the wear trace, it was understood that there was an O content of around 10–15 pct.

Wear trace SEM images of Ni–B/TiC nanocomposite coating with 12 g/l TiC bath concentration at different magnifications are given in Figure 16(d). It was seen that the surface morphology of this sample was slightly different from the other samples. It was noticed that the wear trace was quite superficial in this cauliflower-like surface morphology, which consists of many micro-sized mounds of various sizes. It can be said that in the high magnification SEM image, where the wear trace can be seen more closely, the superficial mounds appear to have been cut or clipped from the tops. As a result of the impressions obtained from the wear trace, it can be argued that the wear mechanism was abrasive and based on the presence of micro-scratches, the micro-cutting mechanism was dominant.[72] In addition, there were black areas in places in the wear trace seen in the SEM image. It is thought that oxidation may have occurred in these parts as a result of exposure to heat. In the EDS analyzes taken from these regions, approximately 7 pct O content was found.[11,27,29,70–73]

IV. CONCLUSIONS

Ni–B/TiC nanocomposite coatings were obtained by reinforcing the Ni–B alloy coatings obtained by adding TMAB to the traditional Watts type Ni bath with TiC particles. The developing properties of nanocomposite coatings deposited on a stainless steel substrate were examined, compared with pure Ni and Ni–B alloy, and the results were presented as follows.

- According to the content analysis and mapping results, it was observed that the TiC particles were successfully deposited into the main structure. While pure Ni has a pyramidal surface structure, a flat structure with sparse circular peaks is observed in Ni–B alloy coatings. Besides that, the TiC particles transformed the surface morphology into a cauliflower-like structure as seen in the SEM images.
- The inclusion of B atoms in the pure Ni main structure caused the disappearance of the other peaks, except for the Ni-specific (111) peak, while these peaks became visible again with the particle reinforcement. It has been understood that successful co-deposition is achieved by the reflection of the (111) and (200) peaks of the TiC particles on the XRD patterns of the nanocomposite coatings. Alloying with B caused a significant decrease in crystal grain size in pure Ni, while TiC reinforcement supported crystallization and caused a slight increase in the grain size of the structure.
- While the microhardness value of pure Ni was measured around 290 HV, this value was found around 400 HV for Ni–B alloy coating. With the reinforcement of TiC, the hardness increased further and the highest hardness value was obtained around 755 HV in the sample with 5 g/l TiC bath concentration. It has been determined that at values higher than 5 g/l TiC bath content, the TiC content in the coating decreases relatively due to possible particle aggregation problems in the bath, and this causes a decrease in hardness.
- In the corrosion analysis, it was concluded that the corrosion resistance of the nanocomposite coating in the worst condition as a result of TiC reinforcement was much superior to that of pure Ni, stainless steel and Ni–B alloy. It was determined that the sample with 12 g/l TiC bath concentration performed 371 pct better than pure Ni and 440 pct better than Ni–B alloy in terms of corrosion current.
- Abrasion analyzes were also carried out and it was observed that the sample with 12 g/l TiC bath concentration decreased by 90 pct in terms of wear volume loss and by 80 pct in average friction coefficient compared to pure Ni. Although plastic deformation and delamination type wear mechanisms are dominant in pure Ni, it has been observed that the abrasive micro-cutting mechanism dominates in nanocomposite coatings. In future studies, the effects of TMAB and current density on the properties of Ni–B/TiC nanocomposite coatings will be examined, and the experimentally obtained microhardness and crystal grain size values of Ni–B/TiC nanocomposite coatings will be tried to be estimated by artificial neural networks (ANN), which is one of the artificial intelligence methods.

ACKNOWLEDGMENTS

The authors thank to the Scientific Research Projects of Çukurova University for financial support of this research (ÇU-BAP, Proje ID: 12868). Electrochemical deposition, analysis and corrosion tests and microhardness measurements were performed in Mustafa Kemal University, Physics Department laboratories, wear tests were performed in Iskenderun Technical University, Metallurgy and Materials Engineering Department laboratories, XRD and SEM analyzes were performed in Çukurova University Central Research Laboratories (ÇUMERLAB). In addition, the authors would like to thank CUMERLAB experts for their help and support.

CONFLICT OF INTEREST

The authors declare that they have no known competing financial interests or personal relationships that could have appeared to influence the work reported in this paper. The authors declare the following financial interests/personal relationships which may be considered as potential competing interests.

REFERENCES

1. Y. Zhang, S. Zhang, Y. He, H. Li, T. He, T. Fan, and H. Zhang: *Surf. Coat. Technol.*, 2021, vol. 421, 127458.
2. A. Tozar and I.H. Karahan: *Surf. Coat. Technol.*, 2020, vol. 381, 125131.
3. K.M. Behbahani, P. Najafisayar, R. Hessam, and N. Zakerin: *Metall. Trans. A*, 2020, vol. 51A, pp. 5475–83.
4. K.M. Behbahani, P. Najafisayar, and M. Pakshir: *Iran. J. Chem. Chem. Eng.*, 2018, vol. 37(5), pp. 117–27.
5. H. Ogihara, K. Udagawa, and T. Saji: *Surf. Coat. Technol.*, 2011, vol. 206, pp. 2933–40.
6. R. Shakoor, R. Kahraman, W. Gao, and Y. Wang: *Int. J. Electrochem. Sci.*, 2016, vol. 11, pp. 2486–512.
7. M. Alizadeh and H. Safaei: *Appl. Surf. Sci.*, 2018, vol. 456, pp. 195–203.
8. Z. Shahri, S.R. Allahkaram, and A. Zarebidaki: *Appl. Surf. Sci.*, 2013, vol. 276, pp. 174–81.
9. M.G. Hosseini, S. Ahmadiyeh, and A. Rasooli: *Mater. Sci. Technol.*, 2019, vol. 35, pp. 1248–56.
10. B. Li, W. Zhang, Y. Huan, and J. Dong: *Surf. Coat. Technol.*, 2018, vol. 337, pp. 186–97.
11. S. Aslan and E. Duru: *J. Mater. Eng. Perform.*, 2022, vol. 31, pp. 1693–704.
12. B.S. Li, Y.X. Huan, H. Luo, and W.W. Zhang: *Surf. Eng.*, 2019, vol. 35, pp. 109–19.
13. E. Unal and I.H. Karahan: *J. Alloys. Compd.*, 2018, vol. 763, pp. 329–41.
14. A. Tozar: *Surf Eng.*, 2020, vol. 36(9), pp. 990–99.
15. E. Unal, A. Yasar, and I.H. Karahan: *Çukurova Univ. J. Fac. Eng. Archit.*, 2021, vol. 36(4), pp. 847–60.
16. F. Dogan, M. Uysal, E. Duru, H. Akbulut, and S. Aslan: *J. Asian Ceram. Soc.*, 2020, vol. 8, pp. 1271–84.
17. D. Li, B. Li, S. Du, and W. Zhang: *Ceram. Int.*, 2019, vol. 45, pp. 24884–93.
18. H.O. Pierson: *Processing and Applications, Handbook of Refractory Carbides and Nitrides Properties, Characteristics*, Noyes Publications, USA, 1996.
19. U. Pandey, R. Purohit, P. Agarwal, S.K. Dhakad, and R.S. Rana: *Mater. Today*, 2017, vol. 4, pp. 5452–60.
20. D. Zhang, J. Li, and J. Zheng: *Mater. Lett.*, 2013, vol. 93, pp. 99–102.
21. B. Li and W. Zhang: *Ultrason. Sonochem.*, 2020, vol. 61, 104837.
22. B. Li, W. Zhang, T. Mei, and Y. Miao: *J. Alloys. Compd*, 2020, vol. 823, 153888.
23. S. Dilek, H. Algul, A. Akyol, A. Alp, H. Akbulut, M. Uysal: J. Asian Ceram. Soc., 2021, vol. 9:2, pp. 673–85.
24. E. Unal, A. Yasar, and I.H. Karahan: *Mater. Res. Express*, 2019, vol. 6, 092004.
25. V.B. Singh and D.K. Singh: *Nanosci. Technol.*, 2014, vol. 1(3), pp. 1–20.
26. K.M. Behbahani, P. Najafisayar, M. Pakshir, and N. Zakerin: *Corros. Eng. Sci. Technol.*, 2019, vol. 54(2), pp. 174–83.
27. M. Demir, E. Kanca, and İH. Karahan: *J. Alloy. Compd.*, 2020, vol. 844, 155511.
28. A. Gunen and A. Curuk: *Adv. Surf. Eng.*, 2020, vol. 72, pp. 673–83.
29. A. Gunen, M. Doleker, M.E. Korkmaz, M.S. Gok, and A. Erdoğan: *Surf. Coat. Technol.*, 2021, vol. 409, 126906.
30. I. Boukhoubza, M. Khenfouch, M. Achehboune, B.M. Mothudi, I. Zorkani, and A. Jorio: *J. Phys.*, 2019, vol. 1292, 012011.
31. N. Zakerin and K.M. Behbahani: *Mater. Today Commun.*, 2021, vol. 27, p. 102327.
32. P. Bindu and S. Thomas: *J. Theor. Appl. Phys.*, 2014, vol. 8, pp. 123–34.
33. M. Saleem, L. Fang, H.B. Ruan, F. Wu, Q.L. Huang, C.L. Xu, and C.Y. Kong: *J. Phys. Sci.*, 2012, vol. 7(23), pp. 2971–79.
34. V. Bilgin, S. Kose, F. Atay, and I. Akyuz: *Mater. Chem. Phys.*, 2005, vol. 94, pp. 103–08.
35. Z.R. Khan, M. Zulfequar, and M.S. Khan: *Mater. Sci. Eng. B*, 2010, vol. 174, pp. 145–49.
36. G.B. Williamson and R.C. Smallman: *Philos. Mag. A*, 1956, vol. 8(1), pp. 34–46.
37. A.L. Patterson: *Phys. Rev.*, 1939, vol. 56, pp. 978–82.
38. O.S. Agboola, E.R. Sadiku, O.I. Ojo, O.L. Akanji, and O.F. Bioditara: *Port. Electrochim. Acta*, 2011, vol. 29, pp. 91–100.
39. R. Orinakova, A. Turonova, D. Kladekova, and R.M. Smith: *J. Appl. Electrochem.*, 2006, vol. 36, pp. 957–72.
40. R.A. Shakoor, R. Kahraman, U.S. Waware, Y. Wang, and W. Gao: *Mater. Des.*, 2014, vol. 59, pp. 421–29.
41. I. Mizusihima, P.T. Tang, H.N. Hansen, and M.A.J. Somers: *Electrochim. Acta*, 2005, vol. 51(5), pp. 888–96.
42. Y. Zhou, S. Zhang, L. Nie, Z. Zhu, J. Zhang, F. Cao, and J. Zhang: *Trans. Nonferrous Met. Soc. China*, 2016, vol. 26(11), pp. 2976–87.
43. N. Guglielmi: *J. Electrochem. Soc.*, 1972, vol. 119(8), pp. 1009–12.
44. E. Unal and I.H. Karahan: *Surf. Coat. Technol.*, 2018, vol. 333, pp. 125–37.
45. E.M.P. Soriano, C.M.A. Mora, and I.M. Meléndez: In situ titanium composites: XRD study of secondary phases tied to the processing conditions and starting materials, inelastic X-ray scattering and X-ray powder diffraction applications. *IntechOpen*, 2019, https://doi.org/10.5772/intechopen.88625.
46. N.D. Banu, I. Banu, and M.S. Katsiotis: *Chem. Pap.*, 2016, vol. 70(11), pp. 1503–11.
47. Z. Abdullaeva, E. Omurzak, and C. Iwamoto: *RSC Adv.*, 2013, vol. 3, p. 513.
48. G. Gyawali, H.S. Kim, K. Tripathi, and T.H. Kim: *J. Mater. Sci. Technol.*, 2014, vol. 30(8), pp. 796–802.
49. Y.N. Bekish, S.K. Poznyak, L.G. Tsybulskaya, and T.V. Gaevskaya: *Electrochim. Acta*, 2009, vol. 55, pp. 2223–31.
50. G. Gyawali and S.W. Lee: *Ceram. Proces. Res.*, 2015, vol. 16(2), pp. 213–17.
51. Y. Wang, S. Wang, X. Shu, W. Gao, W. Lu, and B. Yan: *J. Alloys Compd.*, 2014, vol. 617, pp. 472–78.
52. H.H. Sheu, Y.C. Tzeng, and J.H. Syu: *Mater. Lett.*, 2019, vol. 238, pp. 275–77.
53. Y. Tao, F. Ma, M. Teng, Z. Jia, and Z. Zeng: *Appl. Surf. Sci.*, 2019, vol. 492, pp. 426–34.
54. M. Kallel, M. Masseoud, S. Vesco, M. Barletta, and K. Elleuch: *Ceram. Int.*, 2020, vol. 46(3), pp. 3767–76.
55. K. Krishnaveni, T.S.N.S. Narayanan, and S.K. Seshadri: *J. Alloys Compd.*, 2008, vol. 466, pp. 412–20.
56. H. Ogihara, M. Safuan, and T. Saji: *Surf. Coat. Technol.*, 2012, vol. 212, pp. 180–84.
57. A. Tozar: Coating of low carbon steel with ecofriendly ZnNi/PANI conducting polymer and corroson behaviour investigation

of coated steel, Master's Thesis, Institute of Science and Technology, 2012, Mustafa Kemal University.
58. N. Zakerin and K.M. Behbahani: *J. Mol. Liq.*, 2021, vol. 333, 115947.
59. S. Waware and N.P. Wasekar: *J. Mater. Sci. Eng.*, 2017, vol. 6, p. 6.
60. U.S. Waware, A.M.S. Hamoudaa, and N.P. Wasekar: *Surf. Coat. Technol.*, 2018, vol. 337, pp. 335–41.
61. S. Kasturibai and G.P. Kalaignan: *Mater. Chem. Phys.*, 2014, vol. 147, pp. 1042–48.
62. B. Li, W. Zhang, Y. Huan, and J. Dong: *Surf. Coat. Technol*, 2018, vol. 337, pp. 186–97.
63. K.D. Ralston and N. Birbilis: *Corros. Sci.*, 2010, vol. 66(7), pp. 075005–13.
64. Y. Ozmen and S. Jahanmir: *Pamukkale Univ. J. Eng. Sci.*, 2015, vol. 21(8), pp. 337–43.
65. G. E. Agdacı: Friction and wear behavior of cast iron-nickel aluminide-bronze laminate composite. Master's Thesis, Institute of Science and Technology, 2019, Eskişehir Osmangazi University.
66. M. Zhang, R. Li, T. Yuan, X. Feng, L. Li, S. Xie, and Q. Weng: *Powder Technol.*, 2019, vol. 343, pp. 58–67.
67. W.D. Callister and D.G. Rethwisch: *Materials Science and Engineering*, Wiley, New York, 2011.
68. K.R. Sriraman, S.G.S. Raman, and S.K. Seshadri: *Mater. Sci. Eng. A*, 2006, vol. 418, pp. 303–11.
69. J.H. Liu, J.X. Yan, Z.L. Pei, J. Gong, and C. Sun: *Surf. Coat. Technol.*, 2020, vol. 404, 126476.
70. A. Curuk: The investigation of high temperature wear corrosion behaviors of shower table rolls covered by different coating techniques. Master's Thesis, Institute of Science, Technology and Engineering, 2017, İskenderun Technical University.
71. A. Gunen, E. Kanca, M.S. Karakas, V. Koc, M.S. Gök, Y. Kanca, A. Çürük, and M. Demir: *Surf. Coat. Technol.*, 2018, vol. 348, pp. 130–41.
72. M.S. Karakas, A. Gunen, C. Carboğa, Y. Karaca, M. Demir, Y. Altınay, and A. Erdogan: *J. Alloys. Compd.*, 2021, vol. 886, 161222.
73. R. Tima and F. Mahboubi: *Surf. Coat. Technol.*, 2021, vol. 415, 127084.
74. D. Gultekin, E. Duru, and H. Akbulut: *Surf. Coat. Technol.*, 2021, vol. 422, 127525.
75. I. V. Kragelsky: Friction Wear Lubrication, Tribology Handbook Elsevier Ltd., 1981.
76. M.S. Gok, Y. Kucuk, A. Erdogan, M. Oge, E. Kanca, and A. Gunen: *Surf. Coat. Technol.*, 2021, vol. 328, pp. 54–62.

Publisher's Note Springer Nature remains neutral with regard to jurisdictional claims in published maps and institutional affiliations.

Springer Nature or its licensor (e.g. a society or other partner) holds exclusive rights to this article under a publishing agreement with the author(s) or other rightsholder(s); author self-archiving of the accepted manuscript version of this article is solely governed by the terms of such publishing agreement and applicable law.